Eidgenössische Technische Hochschule Zürich
Swiss Federal Institute of Technology Zurich

Design and simulation of a superconducting qubit coupled to a bulk acoustic wave resonator

Semester Thesis

Jonathan Knoll
jknoll@phys.ethz.ch

Laboratory for Solid State Physics
Departement of Physics, D-PHYS
ETH Zürich

Supervisors:
Prof. Yiwen Chu
Uwe von Lüpke

May 24, 2022

Abstract

Quantum computers promise large speed-ups for certain algorithms which makes them a topic of great interest in research and industry [1]. One common physical implementation of quantum bits are superconducting circuits. We use superconducting qubits in the transmon regime that are strongly coupled to an acoustic resonator through a piezoelectric layer [2–5]. Before fabricating the transmons, finite element simulations are needed to tune them to the right parameter values and to optimize their designs. We perform finite element simulations in Ansys and add the qubit non-linearity using the python package pyEPR [6]. This thesis provides a python class that automates the calculations performed in Ansys and pyEPR and shows different ways of analyzing the simulation results.

Our current qubit design [5] is analyzed in detail and a design modification is suggested with an increased coupling between the qubit and a phonon mode of the acoustic resonator. Furthermore, the presented methods are applied to evaluate different designs for future experiments. In particular, we investigate a design where the qubit couples to two acoustic resonators as well as a design with an additional metal layer in the acoustic resonator for better directing the electric field. The simulations show promising results which need to be confirmed with real fabricated samples.

Contents

Chapter 1

Introduction

Quantum computers can solve some algorithms much faster than classical computers [1]. They are based on quantum bits (qubits) and there are different physical systems that can realize the qubits such as superconducting circuits, trapped ions, quantum dots, photons, electron spin or nuclear spin. Superconducting qubits are a promising candidate for qubits since they can be flexibly designed and combine fast control with decent coherence times. Having discrete energy levels and coherent oscillations between them, superconducting qubits have a strong analogy to natural atoms and are also called *artificial atoms*. In contrast to natural atoms, artificial atoms can be designed to have specific parameters such as specific transition frequencies or a specific electric dipole moment. This tunability offers a great advantage in the qubit design.

Hybrid quantum systems in which superconducting qubits are coupled to mechanical resonators combine different advantages. Acoustical resonators can be isolated from the environment very well, so high quality factors can be achieved [7]. Because the speed of sound is much smaller than the speed of light, acoustic resonators can be made with a much smaller volume than microwave cavities at the same frequency which is beneficial for scaling. Acoustic resonators can be used as transducers, for storing quantum information, for implementing a quantum RAM [8] or for realizing bosonic quantum error correction codes [9–13]. In our experiments, we use high-overtone bulk acoustic wave resonators (HBARs) that are strongly coupled to a superconducting qubit [2–5].

This thesis systematically investigates the influence of the most relevant geometric parameters of our current qubit design and tries to give an intuition about the related changes. As part of this semester project, a python class was implemented which automates many of the calculations for a faster qubit design and simulation in the future [14]. The report begins with a theory section that explains the type of qubit we use and how its parameters are calculated. The coupling to HBARs is explained and the general procedure of design and analysis is presented. In the main part of the report, first the eigenfrequencies of a simple 3D cavity are simulated as an introduction to Ansys. Then our current qubit design [5] is analyzed in detail and a modification is suggested which increases the coupling to the HBAR with the trade-off of having a lower quality factor. After that, different designs for a qubit that is coupled to two HBARs are analyzed and compared. Then, the effect of adding a metal layer in the HBAR is simulated such that the piezo is located within a plate capacitor. This can be used for largely increasing the coupling while reducing the quality factor just a little bit. The appendix contains the results and plots for additional geometric parameter changes as well as technical notes on the qubit modelling in Ansys.

Chapter 2

Theory

For understanding the simulation results of our qubits in this report, we first discuss the properties of the physical systems that realize our qubits. We quickly discuss the bulk acoustic wave resonators to which we couple our qubit and state the formula for the coupling strength. In the end, we describe the design process of a qubit and list typical design parameters.

2.1. Transmon qubits

One way to build qubits are *charge qubits* (also called *Cooper-pair boxes*) where the basis states are charge states. Charge qubits are built of two superconducting islands which are connected by a Josephson Junction. The states of the charge qubit are represented by the number of Cooper pairs that tunneled through the junction. A disadvantage of a typical charge qubit is that the eigenenergies of the qubit depend on the effective offset charge n_g. For optimal parameters, the qubit has to be operated at sweet spots where n_g is a half-integer in units of $2e$. One improvement of the charge qubit is the transmon where the eigenenergies are in good approximation independent on the offset charge. They do not need to be operated at sweet spots anymore since they are almost insensitive to charge noise. An extensive discussion of transmons can be found in [15] and [16]. Here, we only define and derive the most important parameters that characterize a transmon.

Capacitance and capacitive energy
The total capacitance C_Σ of the transmon is dominated by the gate capacitance C_g between the superconducting islands, as visualized in figure 2.1 a). The capacitance C_J of the Josephson Junction, which comes from its geometry, is chosen much smaller, i.e. $C_J \ll C_g$. The charging energy of one Cooper pair is

$$E_C = \frac{e^2}{2(C_J + C_g)} \equiv \frac{e^2}{2C_\Sigma} \approx \frac{e^2}{2C_g}. \tag{2.1}$$

Critical current
If there is no voltage applied to the Josephson Junction, there is still a DC current $I(t)$ flowing through it which is known as the *DC Josephson effect* [17]. The current depends

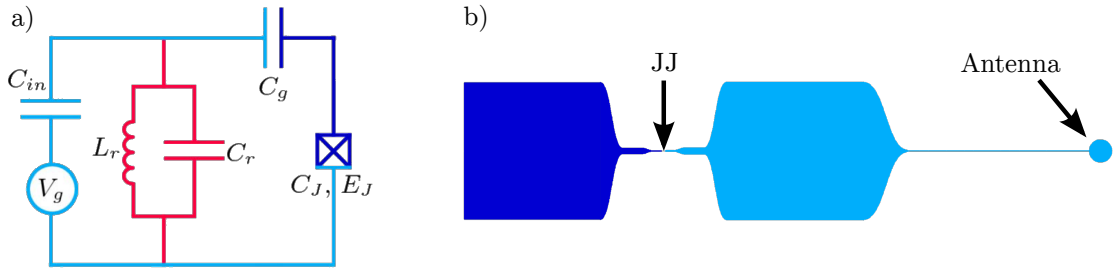

Figure 2.1: **a)** Circuit diagram of our transmon. This is a modified version of a figure from [15]. The two superconducting islands are displayed in light and dark blue respectively. The red part of the circuit represents the readout circuit. In our case, the readout is performed over the coupling between the qubit and the surrounding 3D cavity, so there are no electric circuit elements needed on the qubit chip for the readout. **b)** Our actual transmon design. The two superconducting islands can be seen in two different colors on the left and right, separated by the tiny Josephson Junction (JJ). Our design additionally has an antenna on the right which is used to focus the electric field for coupling to the HBAR as explained later in 2.3.

on the phase difference $\theta_2 - \theta_1$ in the Ginzburg-Landau theory:

$$I(t) = I_c \sin(\theta_2 - \theta_1) \tag{2.2}$$

where I_c is the maximum current that the junction supports at zero voltage and is called *critical current* [18]. It is given by

$$I_c = \frac{\phi_0}{2\pi L_J} \tag{2.3}$$

with $\phi_0 = h/2e$ the flux quantum. The *Ambegaokar–Baratoff formula* offers a way to calculate the critical current by measuring the normal state resistance R_n of the Josephson Junction [19]:

$$I_c = \frac{\pi\Delta}{2eR_n} \tag{2.4}$$

where Δ is the superconducting gap. Measuring R_n is a common technique for determining the inductance $L_j = \phi_0/2\pi I_c$ of the Josephson Junction and from that the Josephson energy.

Josephson energy

The Josephson energy is the energy stored in the Josephson junction when a supercurrent is flowing through it and it is given by

$$E_J = L_J I_c^2 = \frac{\phi_0}{2\pi} I_c = \left(\frac{\phi_0}{2\pi}\right)^2 \frac{1}{L_J}. \tag{2.5}$$

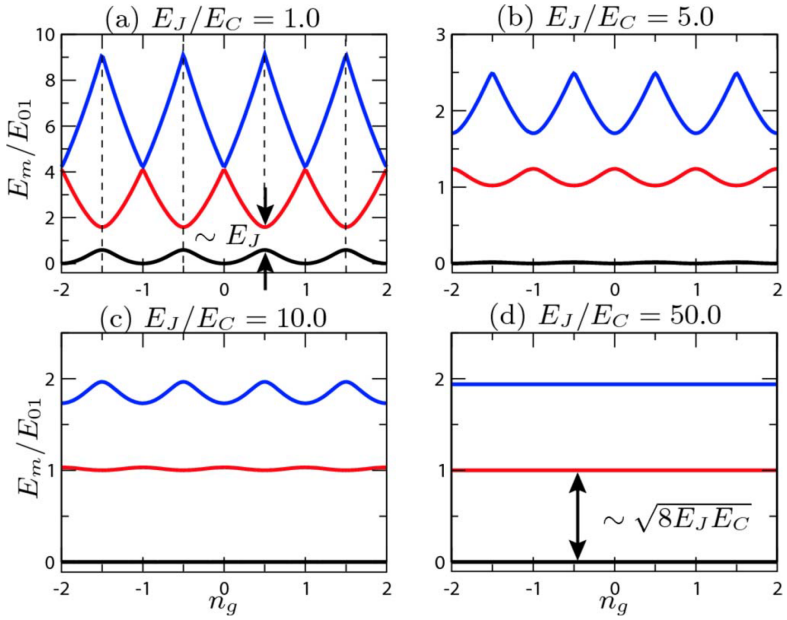

Figure 2.2: Eigenenergies in dependence on the offset charge n_g in units of $2e$ for different ratios of E_J/E_C. The eigenenergies here are normalized with the energy difference E_{01} between ground and first excited state. The transmon regime is roughly $E_J/E_C \geq 50$ where the transmon is practically insensitive to charge noise.

In a transmon, the ratio of Josephson energy E_J to charging energy E_C is greatly increased, typically $E_J/E_C > 50$. Koch et al. show in [15] that an increased E_J/E_C ratio reduces the sensitivity of the transmon to charge noise as seen in figure 2.2.

Eigenenergies

We need to find the eigenenergies of the qubit Hamiltonian for finding the transition frequencies between the qubit states. Koch et al. show in [15] that a transmon can be described by the Hamiltonian

$$\hat{H} = 4E_C(\hat{n} - n_g)^2 - E_J \cos(\hat{\varphi}). \tag{2.6}$$

The eigenenergies of this Hamiltonian are $E_m(n_g) = -E_C a_{2[n_g+k(m,n_g)]} \frac{E_J}{2E_C}$ with $a_\nu(q)$ the Mathieu's characteristic value and $k(m, n_g)$ a function that sorts the eigenvalues. The eigenenergies can be approximated as $E_m \approx -E_J + \sqrt{8E_CE_J}\left(m + \frac{1}{2}\right) - \frac{E_C}{12}(6m^2+6m+3)$ with the Josephson plasma frequency $\omega_p = \sqrt{8E_CE_J}/\hbar$ as explained in [15] in more detail. The energy differences between the first three eigenenergies are

$$E_{01} \equiv E_1 - E_0 \approx \sqrt{8E_CE_J} - E_C \quad \text{and} \quad E_{12} \equiv E_2 - E_1 \approx \sqrt{8E_CE_J} - 2E_C. \tag{2.7}$$

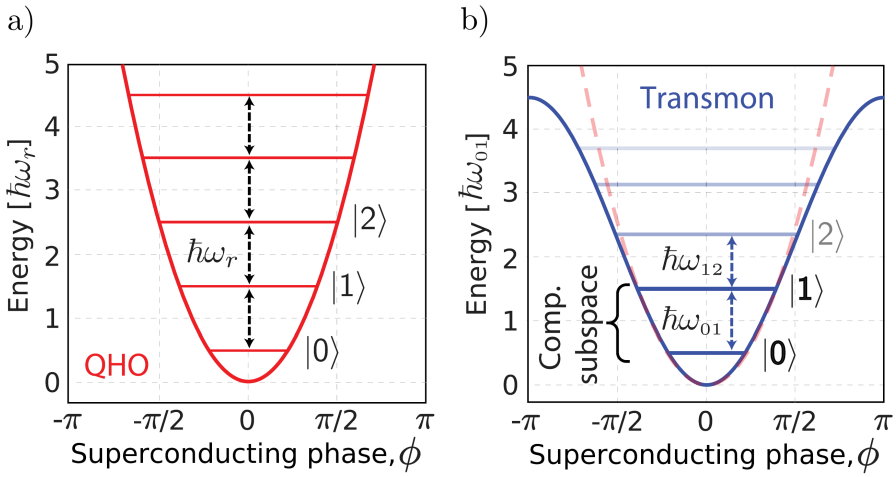

Figure 2.3: **a)** Parabolic potential of a quantum-mechanical harmonic oscillator (QHO) with equal energy level spacing $\hbar\omega_r$. **b)** Potential of a transmon which is sinusoidal due to the non-linear inductance of the Josephson Junction. Here the energy spacing $\hbar\omega_{12}$ is different than the energy spacing $\hbar\omega_{01}$, so we can limit ourselves to the two-dimensional computational subspace of ground and first excited state. The figure is taken from [16].

Anharmonicity

For performing quantum operations, we need to be able to excite the qubit from its ground state to its first excited state with high fidelity. This can be done by applying an electric field where the photons have the energy that corresponds to the energy difference of the ground and first excited state. If we would have a linear inductance L instead of the Josephson Junction, we would have a linear LC resonator which has an equal energy spacing. This means that by applying an electric field, the transmon would not only be excited to its first excited state but to much higher excited states since there are many photons available which all have the right energy to excite the qubit to higher states. But for quantum computing we want to limit ourselves to the two-dimensional subspace of just the ground and first excited state. The Josephson Junction is of great importance because its non-linear inductance changes the potential from a parabola to a sinusoidal potential which results in unequal energy spacings. This is visualized in figure 2.3.

The anharmonicity is defined as the difference between the transition frequencies from the ground to the first excited state and from the first to the second excited state:

$$\alpha = \omega_{01} - \omega_{12} = (E_{01} - E_{12})/\hbar \approx E_C/\hbar \propto \frac{1}{C_\Sigma}. \tag{2.8}$$

Note that we define the anharmonicity in this way such that it is positive. In other literature it is sometimes defined with the opposite sign.

Qubit frequency

It is important to know the qubit frequency for manipulating and reading out the qubit. By *qubit frequency* we mean the transition frequency from ground to first excited state

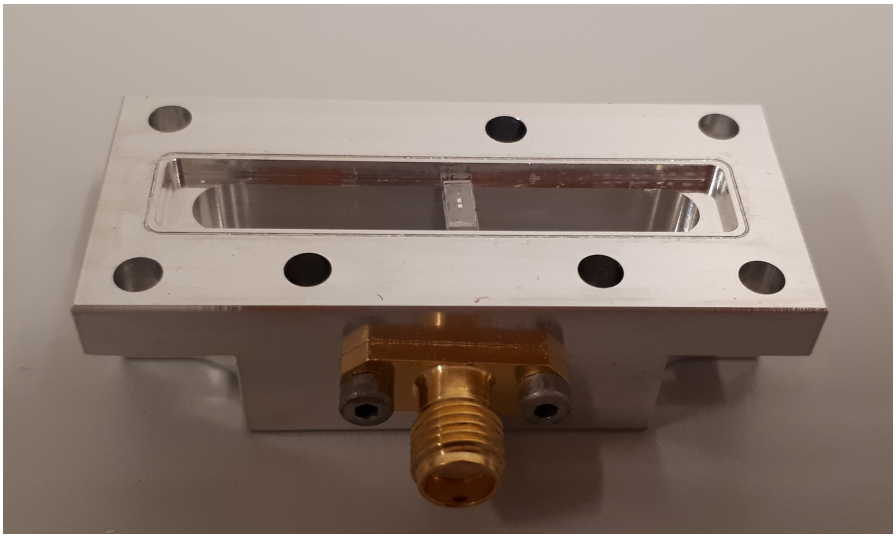

Figure 2.4: Bottom half of the 3D cavity in which the qubit chip is located. The two transparent chips in the middle are the qubit chip and the HBAR chip (which will be introduced in section 2.3). The top half of the cavity, which is not shown here, keeps the qubit fixed and encloses it within a well-defined volume in which the cavity electric field is kept. The adapter in the front is for connecting a cable to the cavity with which microwave signals can be sent into the cavity and received back for manipulating and reading out the qubit. The cavity is made of superconducting aluminum for minimizing dielectric losses. Image credit: Uwe von Lüpke

which is given by

$$\omega_q \equiv \omega_{01} = \frac{E_{01}}{\hbar} = \left(\sqrt{8E_C E_J} - E_C\right)/\hbar \approx \sqrt{8E_C E_J}/\hbar = \frac{2e}{\hbar}\frac{\phi_0}{2\pi}\frac{1}{\sqrt{C_\Sigma L_J}} \propto \frac{1}{\sqrt{C_\Sigma L_J}} \tag{2.9}$$

where we can make that approximation because $E_J/E_C \gg 1$. Note that $\omega_q \propto \frac{1}{\sqrt{C_\Sigma L_J}}$ is what we would intuitively expect since that is the resonance frequency of a classic LC circuit. Further note that this formula is stated for giving an intuition but that in the simulations shown in this report, the frequencies are found numerically by Ansys and not from the formula above.

Coupling between qubit and cavity

We put the qubit in a 3D cavity where they undergo vacuum Rabi oscillations which are described by cavity quantum electrodynamics (cavity QED) and the Jaynes–Cummings model. We use this interaction between qubit and cavity for performing operations on the qubit and reading it out. We denote the vacuum Rabi coupling strength between the qubit and the cavity by g_0 and it is given by

$$g_0 = \frac{1}{\hbar}\vec{E}(\vec{x}) \cdot \vec{d} \tag{2.10}$$

where $\vec{d}$ is the transition dipole moment of the qubit and $\vec{E}(\vec{x})$ is the electric field strength at position $\vec{x}$ [20]. The coupling depends on the electric field strength of the cavity which is strongest in the middle and weaker on the sides. We will later use this by moving the qubit in the cavity in order to change its dispersive shift.

The coupling is largest if the electric field and the dipole moment point in the same direction. If they are perpendicular to each other, the coupling strength is zero. We will later see in section 3.4 that the right alignment of the qubit in the cavity is important.

Dispersive shift

The frequency ω_c of the cavity is shifted when the qubit changes its state. This is important because it enables us to perform a readout of the qubit through the cavity. The difference in single-photon excitation energy of the cavity when the qubit is in state $|0\rangle$ compared to state $|1\rangle$ is called *dispersive shift*. Here we present two ways of calculating it: The dispersive shift we report in the results section is calculated by pyEPR as

$$\chi = p_q p_c \frac{\hbar \omega_q \omega_c}{4E_J} \tag{2.11}$$

with p_m the participation of the junction in mode $m \in \{q, c\}$ [6]. It is calculated as

$$p_m = \frac{\varepsilon_{\text{el}} - \varepsilon_{\text{mag}}}{\varepsilon_{\text{el}}} \tag{2.12}$$

where the total electric field energy ε_{el} and the total magnetic field energy ε_{mag} are computed from the eigenfields phasors as explained in [6].

Because this formula for χ does not provide a good intuition how χ depends on the geometry of the qubit, we quote a second way to calculate it: In the dispersive regime $g_0 \ll \Delta$, the qubit-dependent dispersive cavity shift can be approximated by:

$$\chi \approx \frac{g_0^2}{\Delta} \frac{\alpha}{\Delta + \alpha}. \tag{2.13}$$

with the *detuning* $\Delta := \omega_c - \omega_q$ [15, 21]. In the results section of the report, we show the dispersive shift calculated from pyEPR because this calculation is more accurate but we argue with the formula in (2.13) since that provides a better intuition.

Purcell effect

Because the qubit is coupled to the cavity and the cavity electric field decays with a rate $\kappa > 0$, also the qubit can decay to the transmission line through this interaction with the cavity. This is known as the *Purcell effect*. In the dispersive regime $\Delta \gg g, \kappa$, the qubit decay rate through the Purcell effect becomes approximately [20, 22]

$$\Gamma_c \approx \left(\frac{g}{\Delta}\right)^2 \kappa. \tag{2.14}$$

This decay rate is also called *Purcell limit*.

2.2. Dielectric losses

In the later analysis of the simulation results, it is insightful to look at how much energy is stored in the electric field in different elements of the model such as the cavity, the qubit, the sapphire chips and the piezo. For this, we define the *energy participation ratio (EPR)* P_i of an element i as the ratio of the electrostatic energy W_i stored in that element and the total electrostatic energy W_{total} [23]:

$$P_i = \frac{W_i}{W_{\text{total}}}. \tag{2.15}$$

Furthermore, this definition is important because the open-source Python package pyEPR [6] which we use for calculating the qubit parameters is based on these energy participation ratios. The electrostatic energy stored in volume V_i is

$$W_i = \frac{1}{2}\varepsilon_i \int_{V_i} |\vec{E}|^2 dV \tag{2.16}$$

with $\varepsilon_i = \varepsilon_0 \cdot \varepsilon_{r,i}$ and $\varepsilon_{r,i}$ the relative permittivity of the material of this volume V_i. The *dielectric loss rate* of element i is defined as

$$\Gamma_i = \tan(\delta_i)\, \omega\, P_i \tag{2.17}$$

and the total dielectric loss rate is

$$\Gamma_{\text{total}} = \sum_i \Gamma_i = \sum_i \tan(\delta_i)\, \omega\, P_i. \tag{2.18}$$

The factor $\tan(\delta_i)$ is called *dielectric loss tangent*. Vacuum has a loss tangent of 0. For the bulk medium of sapphire, literature suggests its loss tangent is around $2 \cdot 10^{-8}$ [24] but we conservatively assume a loss tangent of 10^{-7}. Bulk aluminium nitride (AlN), which is the piezoelectric material we use, has a loss tangent of around 10^{-3} [25]. For the surface layers of the qubit we also assume a loss tangent of 10^{-3} [23]. The piezo and the surface layers have a small volume compared to the other elements and because the EPR is given by a volume integral, also their EPRs will be small. But because of the high loss tangents of the piezo and the surface layers, they can still have significant dielectric loss rates.

Note that often the loss rate Γ is reported in $\text{rad}\,\text{s}^{-1}$, so the factor 2π from $\omega = 2\pi f$ is absorbed into the unit instead of into the number. Alternatively, one can also report $\frac{\Gamma}{2\pi}$ in units s^{-1} or one can write for example $\Gamma = 2\pi\, 200\,\text{kHz}$. The relaxation time T_1 of a qubit is

$$T_1 = \frac{1}{\Gamma} \tag{2.19}$$

and is always reported in units of time, so here the factor of 2π has to be taken into account in the calculation.

Surface energy participation ratios

The above expressions for dielectric losses were given for the losses inside volumes. Some elements like the qubit are just very thin layers of material. We can assume that the electric field does not vary largely along the direction of the small dimension. Other examples next to the qubit are the surface layers of materials where the material is not pure but other elements such as oxide layers or dirt are attached to the surface. Furthermore, for materials that are cut from a crystal, the surface will not have the same regularity as the bulk material, resulting in a different dielectric loss tangent. Because of the different loss tangent, we treat surfaces separately.

Since the layers we are considering are very thin, we assume the electric field is constant over the small thickness and we take the thickness h out of the integral to get a surface integral:

$$W_i = \frac{1}{2}\varepsilon_i h \int_{A_i} |\vec{E}|^2 dS \tag{2.20}$$

where A_i is the total surface area. In our case, the surfaces between different materials are the surface of the qubit chip, i.e. the boundary layer between sapphire and vacuum, the boundary layer between qubit and sapphire and between qubit and vacuum. We assume a thickness of $h = 3\,\text{nm}$ for all surfaces [23].

Quality factor

The inverse of the loss tangent is known as the *quality factor* or *Q factor*:

$$Q = \frac{1}{\tan(\delta)}. \tag{2.21}$$

The quality factor corresponds to the initial energy stored in the system, divided by the energy which is lost in one radian of the oscillation cycle. A high quality factor means that the loss rate is low and the oscillation amplitude is only slowly decreasing.

When comparing different qubit designs later in this report, we are interested in qubits with long relaxation times T_1. However because T_1 is the inverse of the total loss rate and the dielectric loss rates of the qubit are proportional to its frequency ω_q, the T_1 time depends on the qubit frequency. Because ω_q changes when modifying the qubit geometry, often it is more insightful to compare the quality factor of two qubit designs instead of the T_1 time since the quality factor is independent on the frequency.

Note on the reported loss rates and T_1 times

In the rest of the report, we are describing the influence of many geometric parameters on the qubit loss rate and T_1 time. It is important to emphasize that our calculations consider only dielectric losses, both in bulk mediums as well as surface losses. There are many other loss mechanisms which we do not consider here. Therefore the reported loss rates are only lower limits and the reported T_1 times upper limits. However, the calculated T_1 times are actually lower than what we measure on our current qubits. This suggests that we overestimate the dielectric loss tangents.

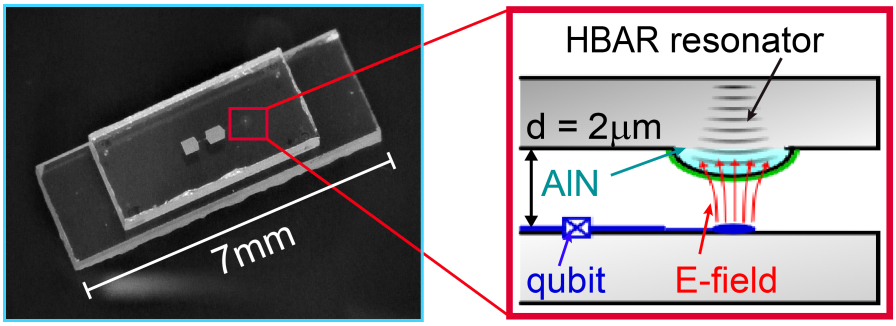

Figure 2.5: Left: The larger qubit chip is visible below the smaller HBAR chip. Both chips are made of transparent sapphire and the qubit made of aluminum is visible on the surface of the qubit chip. **Right:** Sketch of a cross section through qubit and HBAR chip. The HBAR resonator is a plano-convex resonator where on the bottom side of the HBAR chip, there is a sapphire dome than confines the phonon modes. On top of the dome there is a thin layer of aluminum nitride (AlN) which is piezoelectric. The antenna, which is connected to the qubit, focuses the electric field to the piezo. In the piezo, the electric field of the transmon creates mechanical stress which acts on the strain field of the phonon modes. Image credit: Uwe von Lüpke

2.3. Coupling to a bulk acoustic wave resonator

We couple our qubits to high-overtone bulk acoustic wave resonators (HBARs) which are plano-convex resonators made of sapphire that are coupled to the qubit through a piezoelectric material as depicted in figure 2.5. The coupling strength between the electric field from the qubit and the phonon mode is the volume integral over the product of stress and strain:

$$\hbar g_{mn} = \int_V \sigma(\vec{x}) S_{mn}(\vec{x}) dV \tag{2.22}$$

where the strain in the direction we are interested in is $\sigma(\vec{x}) = c_{33} d_{33}(\vec{x}) E(\vec{x})$ [2]. Here c_{33} and d_{33} are the components of the stiffness tensor and the piezoelectric tensor along the z-direction respectively. The phonon modes in our acoustic cavity have a Hermite-Gaussian mode profile. The strain field of the m, n phonon mode is

$$S_{mn}(x,y,z) = \frac{S_0}{r_0}\sqrt{\frac{1}{2^m 2^n m! n!}} \exp\left(-\frac{(x-x_0)^2+(y-y_0)^2}{2r_0^2}\right) H_m\left(\frac{x-x_0}{r_0}\right) H_n\left(\frac{y-y_0}{r_0}\right) \sin\left(\frac{2\pi k z}{L}\right)$$

where L is the thickness of the piezoelectric layer and $k \in \mathbb{N}$. The energy of the phonon mode has to be

$$E_{\text{strain}} = \int_{-\infty}^{\infty} dx \int_{-\infty}^{\infty} dy \int_0^L dz \frac{c_{33}}{2} |S_{mn}(x,y,z)|^2 \stackrel{!}{=} \hbar\omega. \tag{2.23}$$

By evaluating the integral, one finds that the normalization constant is

$$S_0 = \sqrt{\frac{4\hbar\omega}{\pi c_{33} L}}. \tag{2.24}$$

Assuming d_{33} is constant within the piezo, the coupling is

$$\hbar g_{mn} = c_{33} d_{33} \int_V E(x,y,z) S_{mn}(x,y,z) dV. \tag{2.25}$$

$S_{mn}(x,y,z)$ can be evaluated numerically and the integral we approximate as a sum of terms $E(x,y,z)S_{mn}(x,y,z)dV$ for a certain set of coordinates (x,y,z) at which $E(x,y,z)$ was exported from the Ansys simulations and imported into python.
Note that for distinguishing the different couplings, we use g_0 for the coupling strength between qubit and microwave cavity and g for the coupling between the qubit and the S_{00} acoustic mode which corresponds to g_{00} from eq. (2.25).

2.4. Design process and analysis

Here, we quickly describe the qubit design and analysis process and how the simulation results from this thesis are obtained. The qubit is usually designed in two dimensions with a software such as gdspy. It is then exported into Ansys for performing simulations. This way, the qubit geometry cannot be changed much in Ansys. Therefore we completely design the qubit in Ansys so that every geometry parameter can be changed. The modelling of curved parts of the qubit with Bézier curves is described in appendix B. Modelling our simple transmon in Ansys is possible while for larger circuits this quickly becomes impractical.

After modelling the qubit completely in Ansys, one can perform *sweeps* where Ansys HFSS simulates the model for a range of design parameter values. The qubit parameters are then calculated with the python package pyEPR [6] which is necessary because Ansys does not include the anharmonicity introduced by the Josephson Junction. For calculating the coupling, the electric field strength in the z direction is exported for a grid of coordinates around the piezo and stored in text files. They are then imported into Python and the coupling to the $(0,0)$ Hermite-Gaussian mode is calculated according to equation (2.25).

Finally, the volume and surface participation ratios are calculated by integrating the electric field strength squared over the respective volumes. From that the total dielectric loss rate is calculated and with the inverse we get a limit on the T_1 time by dielectric losses. This calculation is controlled by a python script that accesses the Ansys field calculator.

This whole analysis of the qubit parameters was automated through a python class as part of this thesis. When creating the corresponding qubit object, a number of arguments has to be specified such as filenames and Ansys project and design name as well as the names of the different design elements in Ansys. Then all calculations are automatically

performed, the plots of the thesis are created and all results and plots are archived automatically for later use. The code can be found in [14].

Design goals

When designing a qubit by oneself, it might be useful to use the following values as an orientation of what the parameters should roughly be: The cavity frequency needs to be high enough such that it is well above the qubit frequency. Typically, we have cavity frequencies of $\omega_c = 8 - 9\,\mathrm{GHz}$. The qubit frequency ω_q has to be well below the fundamental frequency ω_c of the cavity. Typically, $\omega_q \approx 6\,\mathrm{GHz}$. This ensures $\Delta = \omega_c - \omega_q \gg g_0$ with g_0 the coupling between qubit and cavity.

Also, we want a small charge dispersion because that leads to a reduced sensitivity to charge noise. This is satisfied if the capacitance E_C is chosen large enough so that $E_J \gg E_C$ as explained in detail in [15]. For larger anharmonicities α, there is less leakage to higher qubit energy levels which allows shorter control pulses and larger anharmonicities provide better isolated two-level systems [15]. On the other hand, we want that the charging energy $E_C \approx \hbar\alpha$ is small such that we have $E_J \gg E_C$. Additionally, achieving large anharmonicities requires a small capacitance C_Σ. As we will later see a small capacitance increases the electric field strength at the qubit, leading to higher dielectric losses. So there has to be made some trade-off when finding the ideal anharmonicity. Typically, the anharmonicity is on the order of $\alpha \approx 100 - 300\,\mathrm{MHz}$.

On the one hand, we need a large enough dispersive shift for manipulating and reading-out the qubit. In particular it should be larger than the linewidth of the readout. On the other hand, a too large dispersive shift would cause a too strong Purcell effect. We typically have a dispersive shift χ on the order of a few MHz.

Finally, we want a good selectivity, i.e. we want to couple to only one phonon mode which is the $(0, 0)$ Hermite-Gaussian mode. This is achieved if the electric field points as much as possible in the direction perpendicular to the qubit plane and as little as possible in the other two spacial directions. For a good coupling, there has to be a good overlap of the electric field and the phonon strain field in the piezo. Overall, our general goal of the designs is to achieve a large coupling between qubit and the S_{00} phonon mode while having small loss rates or in other words high T_1 times.

Chapter 3

Qubit simulations

In this chapter, the main results of the Ansys simulations are presented together with methods that can be used for analyzing future qubit designs. First, the eigenmodes of our 3D cavity are theoretically estimated and then simulated with Ansys. Afterwards, our current transmon design is analyzed. Two geometry parameters, the width of the right pad and the length of the left pad, are discussed here in detail while the influence of all other parameters is described in the appendix. Furthermore, different designs for a qubit with two antennas for coupling to two HBARs are presented and compared. The chapter is concluded by showing what benefits it would have to add a metal layer in the HBAR.

3.1. Eigenmodes of a cavity

Before simulating an actual transmon, we draw only the cavity in Ansys and calculate its fundamental frequency while varying the length of one side. This should give a first introduction into Ansys and confirm that these basic calculations are working. In the Ansys model, we already include the qubit and HBAR sapphire chip but without the actual qubit. The cavity geometry and its dimensions are shown in figure 3.1. The cavity is modeled by a box of 30.48 mm × 17.78 mm × 5 mm, united with two cylinders on two sides with heights of 17.78 mm and diameters of 5 mm. At half the height, the cavity is made 1 mm larger in the two horizontal directions as seen in figure 3.1. In this indentation, the qubit chip with a length of 7 mm can be fixed. All used dimensions can be defined as *design properties* in Ansys in order to change them in *sweeps*. In a sweep, one or more properties of the design are changed from a start value to an end value with a step size that can be chosen. For each configuration, Ansys is doing a complete electromagnetics simulation and it can store the calculated fields for later analysis, for example with pyEPR.

First, we derive what the fundamental frequency must be for the simplified case of a rectangular cavity. The electric field of a metal cavity must satisfy the boundary condition that the parallel components of the electric field must be zero at all walls. If we simplify our cavity geometry and assume it is a box of sizes a, b and c in x, y and z direction respectively, these boundary conditions are satisfied for an electric field with

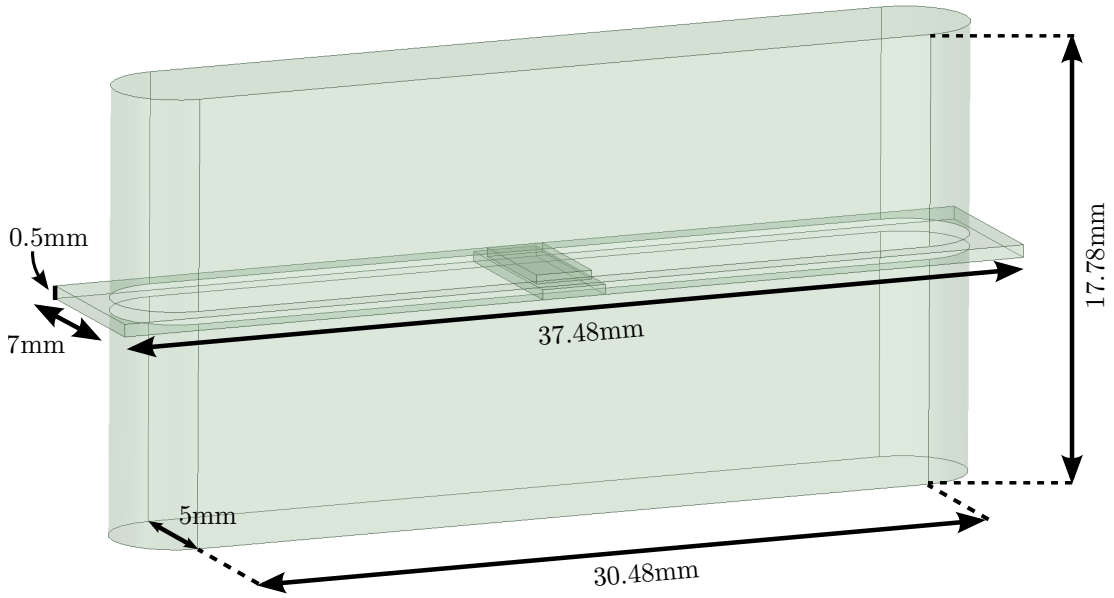

Figure 3.1: Drawing of the cavity with its dimensions.

components

$$\begin{aligned} E_x(x,y,z,t) &= E_{x,0}\cos(k_x x)\sin(k_y y)\sin(k_z z)e^{i\omega t} \\ E_y(x,y,z,t) &= E_{y,0}\sin(k_x x)\cos(k_y y)\sin(k_z z)e^{i\omega t} \\ E_z(x,y,z,t) &= E_{z,0}\sin(k_x x)\sin(k_y y)\cos(k_z z)e^{i\omega t} \\ \text{with } k_x &= \frac{\pi}{a}n, \quad k_y = \frac{\pi}{b}m, \quad k_z = \frac{\pi}{c}l. \end{aligned} \tag{3.1}$$

In order to satisfy the wave equation $\nabla^2\vec{E} - \frac{1}{v^2}\frac{\partial^2\vec{E}}{\partial t^2} = 0$ with v the speed of light, the wave vector must be

$$\vec{k}^2 \equiv k_x^2 + k_y^2 + k_z^2 = \frac{\omega^2}{v^2} \tag{3.2}$$

from which it follows

$$\omega_{nml} = \pi c\sqrt{\frac{n^2}{a^2} + \frac{m^2}{b^2} + \frac{l^2}{c^2}}. \tag{3.3}$$

For our application, we are only interested in the lowest possible frequency of the cavity and have to make sure that it is significantly larger than the qubit frequency. The smallest frequency is obtained for the smallest possible values of n, m and l. Only one of them can be zero because for two or three of them being zero, the electric field would be zero everywhere according to 3.1. If we assume the smallest side of the cavity is side

b in y direction, the smallest frequency is

$$\omega_{101} = \pi c \sqrt{\frac{1}{a^2} + \frac{1}{c^2}}. \tag{3.4}$$

In our case, we ignore the curvature on two faces due to the cylinders and assume we have a rectangular cavity with $a = 30.48\,\text{mm}$, $b = 5\,\text{mm}$ and we sweep the height c between 10 mm and 50 mm. Figure 3.2 shows the simulation results of Ansys together with the theoretical frequencies of a rectangular cavity. We see that for large sizes, the simulation reproduces the theoretical values very well. For small sizes there is a larger deviation because we did not consider the more complex geometry of the cavity as well as the two sapphire chips of qubit and HBAR in our simple rectangular model.

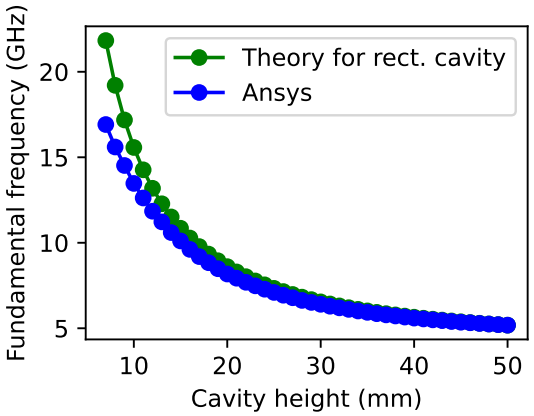

Figure 3.2: Sweep of the cavity height b with the fundamental frequency found by Ansys in blue together with the theoretical values for a rectangular cavity according to equation 3.4 in green. $a = 30.48\,\text{mm}$ and $b = 5\,\text{mm}$ are fixed during the sweep.

3.2. Basic transmon

As an important part of this report, we sweep all essential geometric parameters of our current transmon design and describe their influence on the properties of the qubit. The sweep parameters are illustrated in figure 3.3. Usually, the transmon is designed with a separate program such as the python package gdspy and then imported as a GDS file into Ansys. When importing a GDS file into Ansys, one is limited in geometry changes to scaling, moving and rotating elements of the design which is a major restriction. By designing the transmon completely in Ansys, one can sweep all parameters. The transmon consists mostly of rectangles and circles that are easy to draw in Ansys. The curved connections between rectangles of different sizes, which we call *funnels* here, can be modelled in Ansys as parametric surfaces with Bézier curves as described in appendix B. In the following, we describe the influence of the different geometric parameters. We look at the effects of different widths of the right pad and different lengths of the left pad in detail. Analyzing the other parameters follows the same scheme and is done in appendix A.

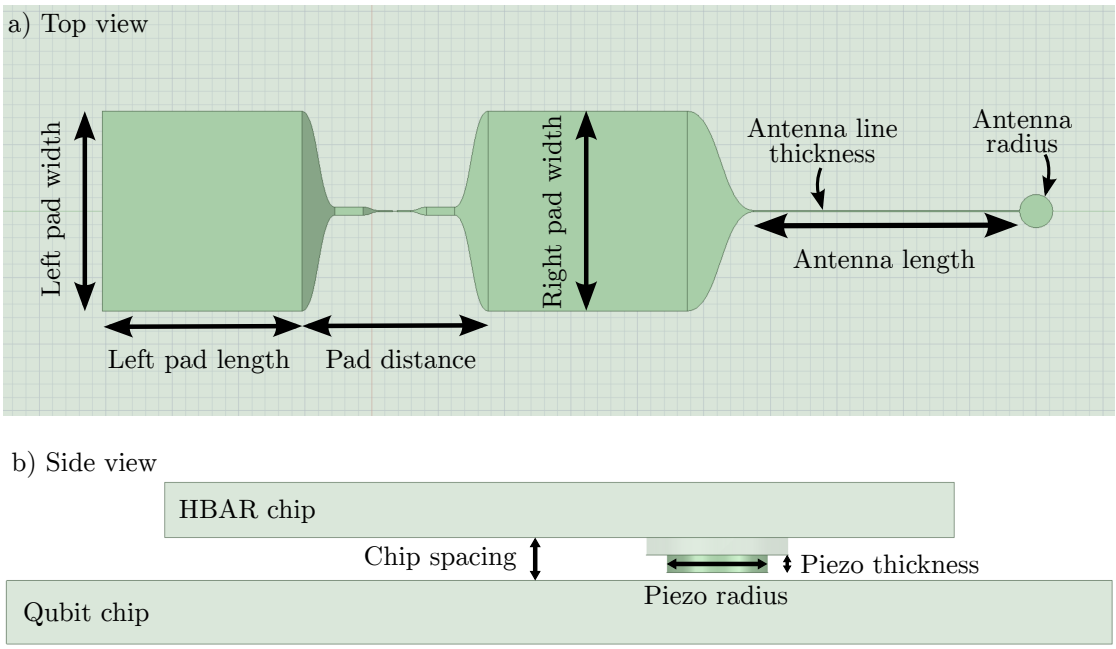

Figure 3.3: Drawing of the qubit in a) top view with proper dimensions and b) side view with exaggerated dimensions for better visibility. The actual sapphire dome is smoothly curved. Because it has a large radius of curvature and is thin compared to the chips, we model the sapphire and piezo dome simply as two cylinders in Ansys.

Sweeping the right pad width

For larger widths of the right qubit pad, we expect that the capacitance increases as for a simple plate capacitor with larger plates. As we derived in section 2.1, the qubit frequency and the anharmonicity scale as $\omega_q \propto 1/\sqrt{C_\Sigma}$ and $\alpha \propto 1/C_\Sigma$ respectively, so both should decrease. The ratio $E_J/E_C \propto C_\Sigma$ should increase. This is confirmed by the simulation results shown in figure 3.4. Furthermore, a large width of the right pad effectively shields the antenna from the electric field and reduces the electric field strength in the antenna and the piezo. This can be seen in figure 3.5 where the electric field strength is plotted for four different pad widths. The lower electric field strength at the antenna leads to a reduced coupling. Because of the lower dielectric loss rate at the piezo, this leads to larger limits T_1^d on the relaxation time. Due to the transfer of charges from the antenna to the right pad with increasing pad width, the average distance between charges and therefore the dipole moment of the qubit as well as the coupling to the cavity decrease. Together with the reduced anharmonicity, this leads to a decrease in the dispersive shift for larger widths of the right pad.

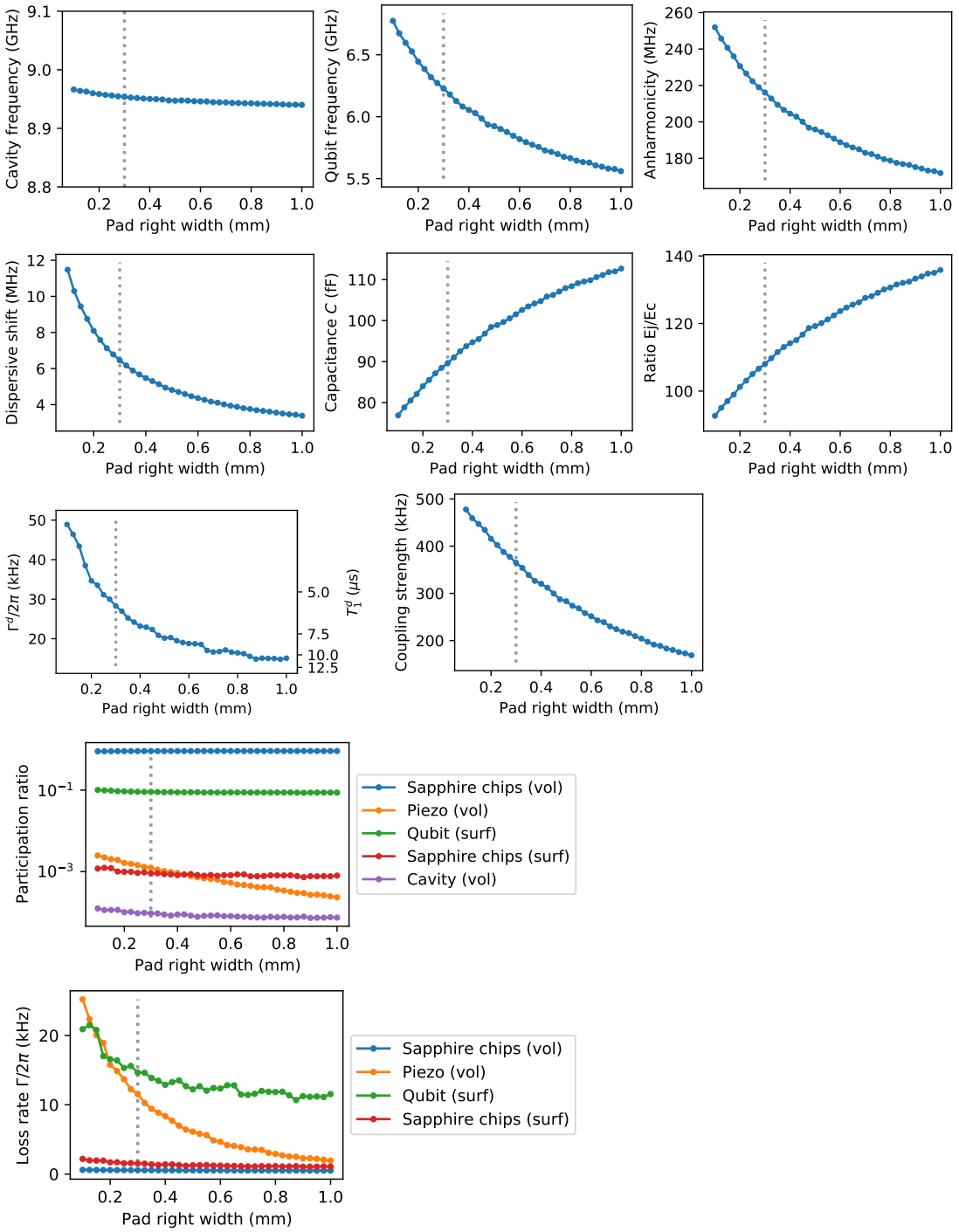

Figure 3.4: Qubit parameters for the sweep of the right pad width. The capacitance increases for larger pad widths as for a plate capacitor. This decreases the qubit frequency and anharmonicity and increases the E_J/E_C ratio. Due to the relocation of charges from the antenna to the right pad, the dipole moment and the dispersive shift decrease. Because of a weaker electric field at the antenna, the loss rates are lower and the relaxation time higher.

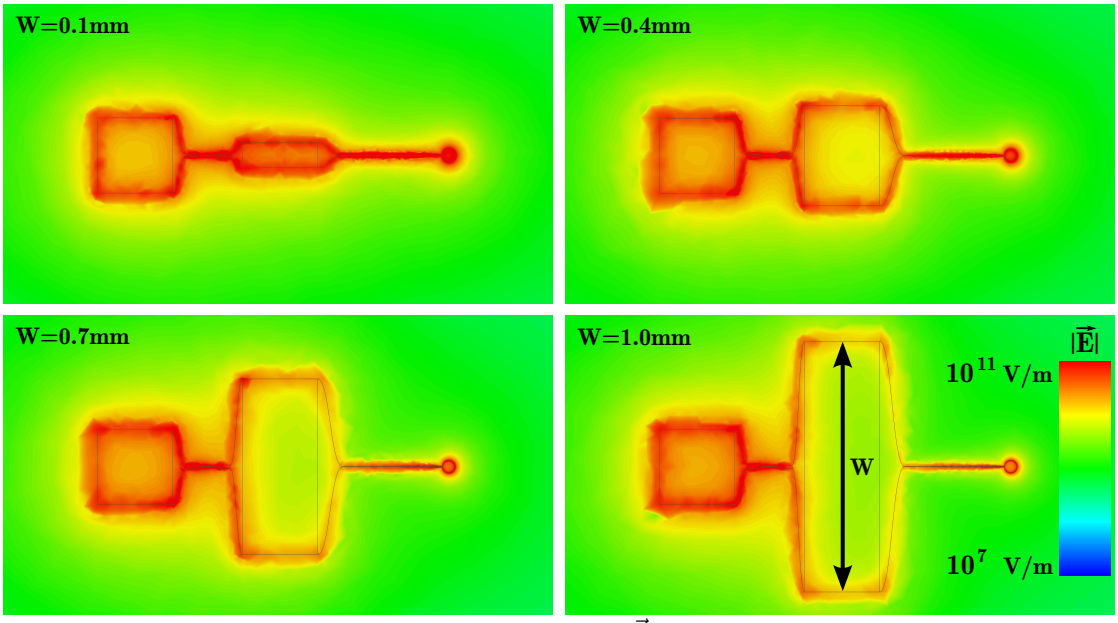

Figure 3.5: Plots of the electric field strength $|\vec{E}|$ in the qubit plane for four different widths of the right pad. On the antenna, $|\vec{E}|$ is decreasing for larger pad widths as the right pad is effectively shielding the antenna. This reduces the coupling and increases the bound T_1^d of the relaxation time. On the bottom right, the logarithmic color scale for the electric field strength is given. The values correspond to the electric field strength when the system is excited with an energy of 1 J. In reality, this would be scaled by a factor $\hbar\omega$.

Sweeping the left pad length

Increasing the left pad length increases the capacitance which leads to a reduction in the qubit frequency and the anharmonicity as seen in figure 3.6. The change in the dispersive shift can be explained with equation (2.13) which reads

$$\chi = \frac{g_0^2}{\Delta}\frac{\alpha}{\Delta+\alpha} \quad \text{with} \quad g_0 = \frac{1}{\hbar}\vec{E}(\vec{x})\cdot\vec{d}. \tag{3.5}$$

In figure 3.6 we see that the dispersive shift has a minimum for a pad length of roughly 30 µm. For larger lengths, it slightly increases because of an increased qubit-cavity coupling g_0 through an increased dipole moment $|\vec{d}|$. For smaller pad lengths, the dispersive shift is strongly increased. This is because the qubit frequency increases, so $\Delta = \omega_c - \omega_q$ decreases. Also the factor $\alpha/(\Delta+\alpha)$ increases because α increases and Δ is much larger than α, so the nominator increases more than the denominator.

The increased coupling strength g between the electric field of the qubit mode and the strain field of the phonon mode must come from an increase of the electric field strength in the direction perpendicular to the qubit plane which we call z direction. This can be due to an overall increased electric field strength $|\vec{E}|$ or due to an improved directionality of the electric field. The coupling is strongest when the electric field points exactly in the z direction across the whole antenna because we are coupling to a longitudinal strain mode in the z direction. In order to check whether the directionality is improved or not, we calculate the following three integrals:

$$W_x := \int_V |E_x|^2 dV, \quad W_y := \int_V |E_y|^2 dV, \quad \text{and} \quad W_z := \int_V |E_z|^2 dV, \tag{3.6}$$

where we integrate over the piezo volume. These integrals are equivalent to the energy stored in the x, y and z component of the electric field, divided by $\frac{1}{2}\varepsilon_0\varepsilon_{r,i}$ with $\varepsilon_{r,i}$ the relative permittivity of the corresponding element i. For simplicity, we denote them with W_x, W_y and W_z, although they differ from the energy by a constant factor. From the ratio of these quantities, one knows if the electric field is pointing more in z direction or not. We plot W_x, W_y and W_z in a logarithmic plot in figure 3.7. The figure shows that the $\log(W_x)$, $\log(W_y)$ and $\log(W_z)$ curves are roughly equally spaced over the sweep. This means that the ratios of W_x, W_y and W_z stay constant. Therefore the directionality of the electric field does not improve. However, we see that all three components increase with

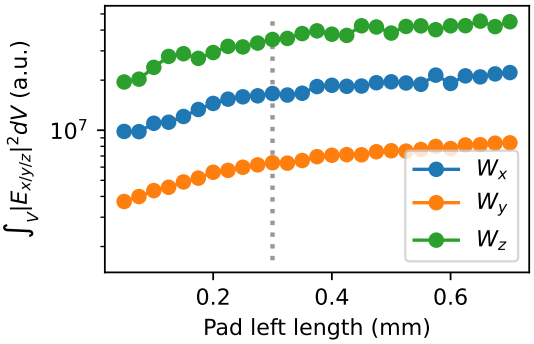

Figure 3.7: Rescaled energy stored in the x, y and z component of the electric field in the piezo dome in arbitrary units and with the y axis in log scale. The total energy increases with larger pad length while the directionality, i.e. the ratios of the electric field strength components, stay constant.

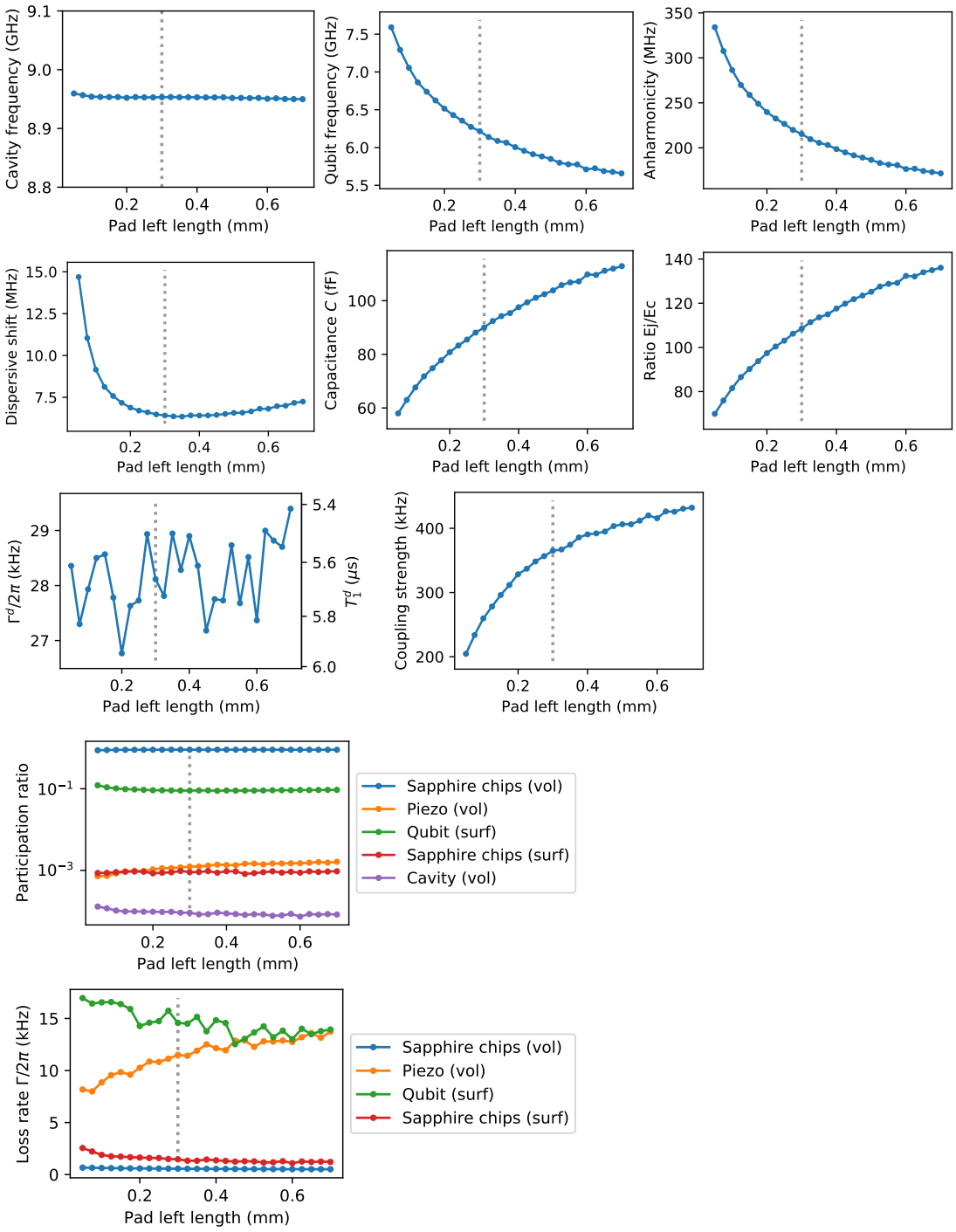

Figure 3.6: Qubit parameters for the sweep of the left pad length. With longer lengths of the left pad, charges are redistributed from the left pad to the antenna. This increases the energy participation ratio of antenna and piezo and therefore increases both the coupling to the piezo as well as the dielectric losses at the piezo. But the loss rate of the left pad is significantly reduced such that the total dielectric loss rate does not change too much, at least for the dielectric loss tangents assumed here. This should be regarded more in a qualitative than a quantitative way since there is a large uncertainty in the actual loss tangents.

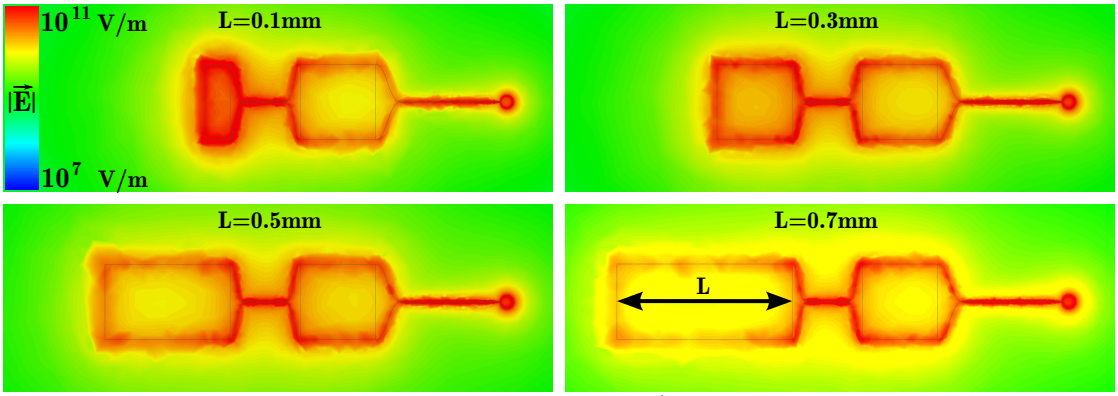

Figure 3.8: Plots of the electric field strength $|\vec{E}|$ on the qubit chip surface for four different lengths L of the left pad. $|\vec{E}|$ is decreasing on the left pad for larger lengths and therefore the energy participation ratio of the pad, which depends on $|\vec{E}|^2$, is also decreasing. On the top left, the logarithmic color scale for the electric field strength is given. The values correspond to the electric field strength when the system is excited with an energy of 1 J. In reality, this would be scaled by a factor $\hbar\omega$.

larger pad lengths. Therefore the total electric field strength $|\vec{E}|$ at the antenna is increasing which leads to a higher coupling strength.

Since the energy participation of piezo and antenna increase, other energy participation ratios must decrease. Analyzing the participation ratios of the individual components of the qubit, we observe that the energy participation of the left pad is decreased. This can be best understood when looking at the electric field strength of the left pad for different lengths as shown in figure 3.8. With increasing pad size, the electric field becomes weaker on the left pad. Because the participation ratio depends on the electric field strength squared, this leads to a significant reduction of the participation ratio of the left pad. The plot of the loss rates in figure 3.6 shows that the change in dielectric loss rate of the piezo and the left pad are similar, so in total the relaxation time T_1^d due to dielectric losses does not change much. Note that this holds only for the dielectric loss tangents that we assumed here.

3.3. Proposal for a modification of our transmon design

Based on the reported findings, we might be able to increase the coupling strength while not decreasing the relaxation time T_1 too much. This can be done by increasing the electric field at the antenna while decreasing it at the left pad. The higher electric field, which is necessary for a stronger coupling, also leads to higher loss rates of the piezo. This can partially be compensated by a reduced loss rate of the left pad so that the T_1 time does not change much. Increasing the pad size leads to a larger capacitance and therefore to a smaller qubit frequency and anharmonicity as well as to a smaller dispersive shift. A smaller anharmonicity is not problematic in our case because it just requires a longer duration of control pulses [15] and the focus of this experiment is more

a good coupling than fast operations. Choosing a final width and length for the left pad is an incremental process where we modify the width and left of the left pad until we reach a combination of high coupling and high T_1 that satisfies us. One could also define a cost function that combines the different qubit parameters into a single score that can be maximized in an optimization. However, this would require us to define coefficients and functions how the individual parameters are scored and this is also not objective but rather an intuitive decision about what is more important for the current parameters.

Based on this iterative approach, we suggest a width of 0.7 mm and a length of 1.3 mm for the left pad. Keeping all other parameters the same compared to the current transmon design, this leads to a 39 % increase in phonon coupling from 363 kHz to 504 kHz. It leads only to a 9 % decrease in the bound T_1^d on the relaxation time from 5.7 µs to 5.2 µs which might be a good trade-off[i].

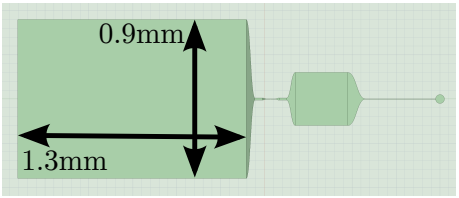

Figure 3.9: Proposed dimensions of the left pad for increasing the coupling strength.

The changes in the other parameters are listed in table 3.1 as design a). In this design, the qubit frequency ω_q is reduced by 20 %. Reducing the qubit frequency immediately decreases the dielectric loss rates which are proportional to ω_q and therefore increases the relaxation time T_1. For a better comparison, one should look at the quality factor Q in table 3.1. The quality factor is reduced by 26 % in design a) compared to the original design. This is what needs to be accepted for a higher coupling. Alternatively for a better comparison, one can also increase the qubit frequency $\omega_q \propto 1/\sqrt{L_J C_\Sigma}$ by decreasing L_J. In order to increase the qubit frequency by 20 % from 5 GHz to e.g. 6 GHz which was an initial design goal, we have to change L_J to $(5/6)^2 L_J$. The corresponding qubit parameters are listed in the same table under design b). The quality factor is only slightly decreased more than in design a) but the T_1 time is drastically reduced by 28 % compared to 8.5 % in design a). The coupling is just slightly increased compared to a). This second proposal b) should emphasize that the real trade-off is between the coupling and the quality factor, not between the coupling and the T_1 time. Depending on the concrete application, it might be useful to use this proposal when a higher coupling is very beneficial and a certain reduction in the T_1 time is acceptable.

[i] After this project was completed, it was found that dielectric losses might not be limiting the relaxation time in our experiments and that particularly phonon radiation should be taken into account. This should be analyzed in more detail but is out of the scope of this report. However when interpreting the results here, one should note that the assumed dielectric loss tangents have a high uncertainty and that we only consider dielectric losses here.

Design	Current	a)	b)
ω_q (GHz)	6.23	5.00 (−20 %)	6.03 (−3 %)
ω_c (GHz)	8.95	8.86 (−1 %)	8.90 (−0.6 %)
α (MHz)	216	131 (−39 %)	114 (−47 %)
χ (MHz)	6.46	7.44 (+15 %)	12.59 (+95 %)
g (kHz)	365	504 (+39 %)	515 (+41 %)
T_1^d (µs)	5.63	5.15 (−8.5 %)	4.07 (−28 %)
C (pF)	89.6	148 (+65 %)	170 (+90 %)
Q^d	35, 100	25, 800 (−26 %)	24, 500 (−30 %)

Table 3.1: Comparison between the parameters of the current transmon design and a new proposal a) with increased left pad length and width. Design b) has the same geometry as a) but the inductance L_J is reduced to increase the qubit frequency for better comparison. It is also helpful to instead look at the limit on the quality factor Q^d by dielectric losses for a comparison independent on the qubit frequency.

3.4. Transmon with two antennas

For future experiments in our group, we want to couple the transmon to two HBARs. The idea is to produce the same HBAR chips as before but having a different transmon with two antennas and a larger qubit chip on which both HBAR chips can be placed. First, we analyze how our transmon design can be modified to have two antennas. One could attach the second antenna either to the same pad as the first antenna or to the other pad. Then the antennas can be bent away in different directions to have space for both HBAR chips. The simplest possibilities for arranging the two antennas on the chips are shown in figure 3.10. Additionally, one can rotate the qubit and HBAR chips. Designs c*) and d*) are equivalent to design c) and d) rotated by 90° respectively. In some cases like a) and b), rotating the design by 90° would result in a design where the dipole moment of the qubit is perpendicular to the electric field of the cavity and therefore the coupling is zero. In the electric field strength plot, one can see that in design b), most charges are concentrated on the lower pad and not on the antennas. Design b) therefore has a high quality factor but low coupling rates. We suggest a design b*) where the lower pad is made larger such that the charges are more concentrated on the antenna rather than the lower pad. This increases the coupling but reduces the quality factor. That situation is analogous to the qubit with just one antenna from the previous section where we increased the length of the left pad for increasing the electric field strength at the antenna.

Comparing the qubit parameters of the different designs in table 3.2, we see that designs a), c), c*) and d) lead to the highest coupling. Under those four designs, c*) is the only design which is rotated such that the two HBAR chips can be moved further apart. In the top left sketch of the cavity in figure 3.10 this would correspond to moving the two HBAR chips to the left and right respectively. In design a), c) and d) one chip is at the top and at the bottom of the sketch so that they cannot be further separated without touching the wall of the cavity. Moving the HBAR chips further apart might be beneficial

Design	a)	b)	b*)	c)	c*)	d)	d*)
ω_q (GHz)	6.00	6.42	4.05	5.49	5.49	5.46	5.42
ω_c (GHz)	8.59	8.47	8.31	8.51	8.48	8.52	8.46
α (MHz)	182	224	82	140	135	129	139
χ (MHz)	18.0	7.11	4.6	6.0	14.2	15.5	6.2
g_1 (kHz)	428	229	380	412	410	416	386
g_2 (kHz)	439	229	378	417	423	418	384
T_1^d (µs)	3.28	10.46	5.3	4.23	3.90	3.65	4.3
C (pF)	106	87	237	138	144	150	139
Q^d	20,500	67,200	21,500	23,200	21,400	19,900	23,300

Table 3.2: Comparison between the parameters of the different design suggestions for the two-antenna chip. Design c*) looks most promising since it has a high coupling, a high T_1 and out of designs a), c), c*) and d) it is the only one where the two HBAR chips can be further separated due to the orientation in the cavity. The seven design variations are shown in figure 3.10.

because the chip edges have some roughness after dicing and they cannot be placed with perfect accuracy on the qubit chip so that there has to be some spacing for technical reasons. Furthermore, because of the rough edges, there might be high dielectric losses on those edges. In order to avoid this, one can move the two HBAR bar chips further apart such that their edges are not so close to the Josephson Junction. Next to design c*), also design d*) offers the possibility to further separate the chips. Design d*) has a bit lower coupling but which is still good. The advantage of d*) is that the antennas are further away from the corners of the HBAR chip where spacers and glue dots are placed. We conclude that from those design suggestions, designs c*) and d*) look the most promising and should further be investigated. They have a high coupling, a high quality factor and they are aligned in the cavity such that the two HBAR chips can be further separated.

For design c*), the dispersive shift is more than twice the value of the current one-antenna transmon which leads to a stronger Purcell effect. But since the dispersive shift is proportional to both the dipole moment and the electric field strength in the cavity, one can move the qubit to the ends of the cavity where the electric field strength is smaller. As we saw in section 3.1, the cavity electric field is strongest in the middle and falls off to the sides of the cavity like $\sin(x)$ for $x \to 0$ or π. This was confirmed in Ansys simulations as well.

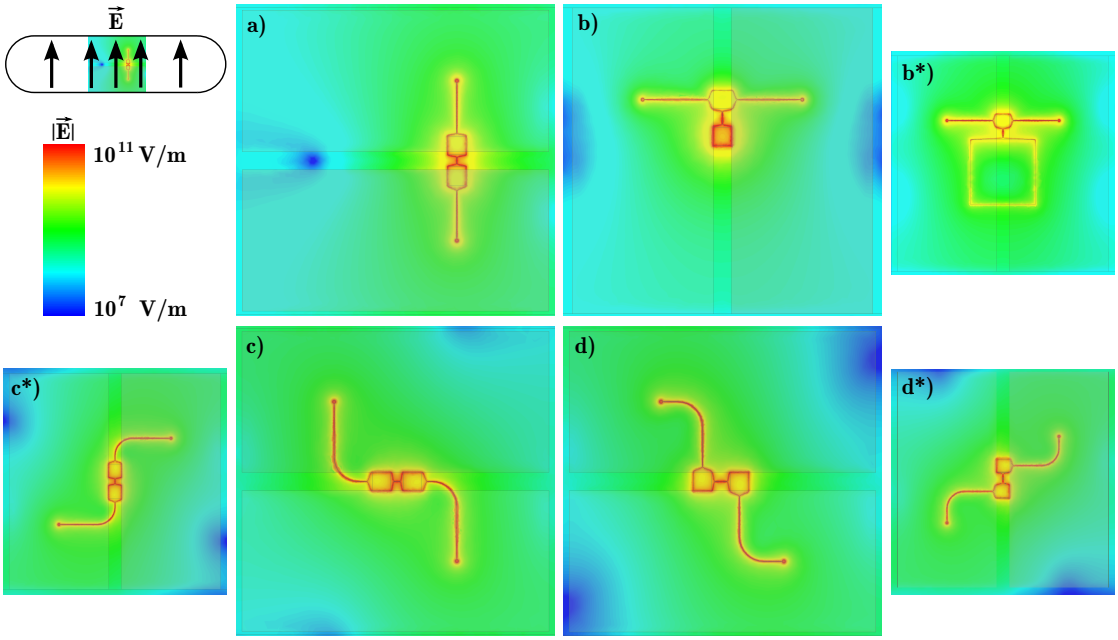

Figure 3.10: Plots of the electric field strength in the qubit plane for different design suggestions with two antennas. On the top left, the cavity is depicted from a top view and the direction of the electric field is sketched. Below, the logarithmic color scale for the electric field strength is given. The values correspond to the electric field strength when the system is excited with 1 J. In reality, this would be scaled by a factor $\hbar\omega$. **a)** Design with the two antennas going away in a straight line from both pads. **b)** Design with the two antennas attached to the same pad. **b*)** Modification of b) with a larger lower pad to increase the coupling. **c)** Design with the two antennas going away in a curved line at both pads. **c*)** Design c), rotated by 90°. **d)** Similar design as c) with the antennas attached to another side of the pad. **d*)** Design d), rotated by 90°. Note that if a) and b) would be rotated by 90°, the coupling between qubit and cavity would be zero because the dipole moment of the qubit would be perpendicular to the electric field of the cavity.

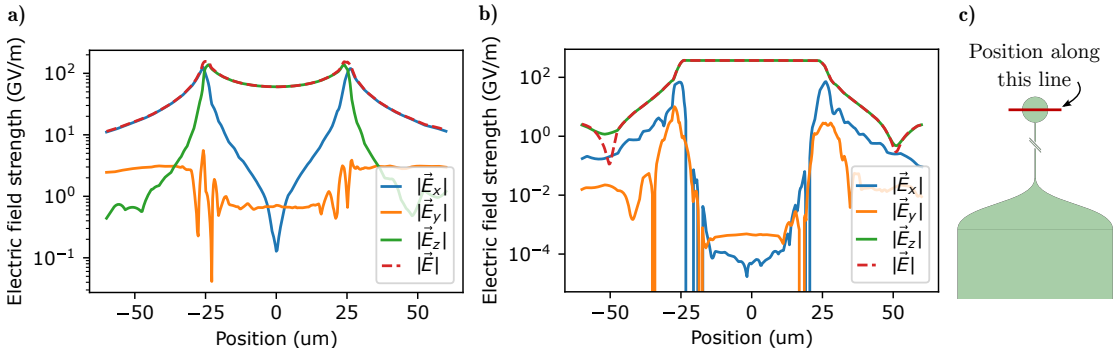

Figure 3.11: Plot of the electric field strength along the diameter of the HBAR dome in y direction as indicated by the red line on the right drawing in c). Position 0 is chosen as the center of the antenna with a radius of 25 µm. **a)** Electric field strength for the current design without a metal layer and **b)** with a metal layer. Because of the metal layer directly above the piezo, the components $\vec{E}_x$ and $\vec{E}_y$ of the electric field parallel to the surface are reduced by a factor of 10^6. Therefore, $\vec{E}_z$ gets larger and is constant over the surface of the antenna. Only at the edge of the antenna at ±25 µm there are small deviations. The electric field strength is simulated by Ansys when the qubit is excited with an energy of 1 J. In reality, this would be rescaled by $\hbar\omega$.

3.5. Metal layer below the piezoelectric layer

Improving the directionality of the antenna electric field, i.e. increasing the electric field strength in the z direction perpendicular to the antenna plane and decreasing its components parallel to the plane, would increase the coupling which depends only on the z component of the electric field. If the total electric field strength $|\vec{E}|$ is kept constant, the energy participation ratio of the piezo which depends on $|\vec{E}|^2$ will also stay the same and therefore also dielectric losses will remain the same. So improving the directionality would be a great benefit for the coupling with no trade-off in the quality factor.

One way to achieve this is to insert a thin metal layer below the piezoelectric layer. This metal layer forms a plate capacitor with the antenna where the piezo is located inside this plate capacitor. In the idealized case of an infinitely large plate capacitor, the electric field should only point in the direction perpendicular to the surfaces which is the z direction in our case. Because the metal layer will be very thin, we simulate it in Ansys as a 2D circle with a perfect conductor boundary condition and with the same diameter as the piezo. The effect on the three components of the electric field can be seen in figure 3.11 where the electric field strength is plotted at half the thickness of the piezo along a straight line through the center of the piezo. In the middle of the piezo, the z component of the electric field is larger by a factor of 10^6 than the x and y components. Close to the edge of the antenna, there are some more complicated effects but still the directionality of the electric field is greatly improved by the metal layer.

Table 3.3 lists the qubit parameters for the current design without a metal layer as well as with a metal layer - denoted by a) in the table - where all other geometry parameters were kept constant. The table shows that the coupling strength was increased by a factor

Design	Current	a)	b)	c)
ω_q (GHz)	6.23	6.10 (−2 %)	5.47 (−12 %)	6.00 (−4 %)
ω_c (GHz)	8.95	8.95 (+0 %)	8.93 (−0.2 %)	8.94 (−0.1 %)
α (MHz)	216	204 (−6 %)	166 (−23 %)	159 (−26 %)
χ (MHz)	6.46	7.30 (+13 %)	3.46 (−46 %)	4.70 (−27 %)
g (kHz)	365	1643 (+350 %)	687 (+88 %)	685 (+88 %)
T_1^d (µs)	5.63	1.34 (−76 %)	6.0 (+7 %)	5.2 (−8 %)
C (pF)	89.6	95 (+6 %)	117 (+31 %)	122 (+36 %)
Q^d	35,000	8,200 (−77 %)	32,800 (−6 %)	31,200 (−11 %)

Table 3.3: Comparison between the parameters of the current transmon design and the qubits with a metal layer below the piezo. **a)** Qubit with the metal layer but otherwise the same geometry. **b)** Qubit with metal layer and increased width of the right pad of 1.2 mm. This shields the antenna such that the coupling is decreased compared to a) but the quality factor is largely increased. **c)** Same geometry as in b) but with smaller Josephson Junction inductance in order to increase the qubit frequency ω_q.

of 4.5 while the relaxation time was reduced by a factor of 4. The EPR of the piezo is increased by a factor of 7 from 0.12 % for the transmon without metal layer to 0.84 % for the transmon with metal layer. The energy stored in the electric field in the piezo volume increases from $1.4 \cdot 10^{-29}$ J to $9.4 \cdot 10^{-29}$ J which is also a factor 7 larger. The electric field strength scales as the square root of the energy, so it should be roughly $\sqrt{7} \approx 2.6$ times larger. The coupling depends on the z component of the electric field strength and it is increased by a factor of 4.5. So it seems like because of the metal layer, there are more field lines going through the piezo than before (factor 2.6) and the remaining factor of $4.5/2.6 = 1.7$ comes from the fact that the electric field is directed more into the z direction and less into the x and y directions than before.

Increasing the coupling by a factor of 4.5 might be more than necessary and one might rather want to have less coupling but a better quality factor. This can be achieved by increasing the width of the right pad which effectively shields the antenna from the rest of the qubit. Thus a larger right pad reduces the electric field strength at the antenna, decreases the coupling and increases the quality factor. Increasing the right pad width from 0.3 mm to 1.2 mm would give a coupling increased by 88 % and a quality factor reduced only by 6 % as listed under design b) in table 3.3. Because the capacitance is increased, the qubit frequency is decreased. Therefore a design c) is listed where the qubit frequency is increased to 6 GHz again by reducing the inductance of the Josephson Junction.

Chapter 4

Conclusion

The goals of this project were accomplished by analyzing our current transmon design in detail, making new design suggestions and providing a tool set for supporting future qubit design and simulation. The provided python class in [14] automates the calculation of qubit and cavity frequency, anharmonicity, dispersive shift, capacitance, E_J/E_C ratio, qubit-phonon coupling strength, EPRs, dielectric loss rates and a limit on the total loss rate and T_1 time through dielectric losses. Furthermore, this thesis gives examples on how to closer analyze the obtained data. For getting an intuition of how the charge distribution on the qubit elements changes in a sweep, one can select single designs of a sweep and plot the electric field around the qubit as in figure 3.5 and 3.8. If one wants to know if the directionality of the electric field is improved, one can calculate the energy stored in the three spacial dimensions of the electric field and see if their ratio changes as in figure 3.7. It can also be insightful to plot the electric field strength along a line going through the qubit as it was done for the design with the metal layer in figure 3.11.

When comparing different design variations, it became clear that it is important to look at the quality factors instead of the T_1 times since the limit on the T_1 time by dielectric losses depends on the qubit frequency. If a certain qubit frequency needs to be established after it was changed in a sweep, it was shown that this can be done precisely by changing the inductance of the Josephson Junction. We saw that increasing the coupling strength between qubit and piezo requires stronger electric fields at the piezo which increases the dielectric losses of the piezo. So there is a fundamental trade-off between a high coupling strength and a high T_1 time when focusing on dielectric losses. The only exception is that one can improve the directionality of the electric field: The x and y component of the electric field do not contribute to the coupling to the $(0, 0)$ longitudinal mode but they do contribute to dielectric losses. Adding a metal layer greatly aligns the electric field at the piezo in the z direction. We do not know the loss tangents very well, so there is a large uncertainty in the calculated loss rates and the limit on the T_1 time. Assuming the loss tangents given in section 2.2, we could increase the coupling rate by 88 % while reducing the quality factor by only 6 % as listed under design b) in table 3.3.

The explained trade-off between qubit-phonon coupling and T_1 is well visible in our current transmon design: We showed that by increasing the left pad size, one can decrease the EPR of the left pad and increase the EPR of the antenna. This increases the coupling strength but also increases the total dielectric loss rate. But the dielectric losses at the surface of the qubit are significantly reduced so that the total loss rate does not increase as much as otherwise expected. For some experiments, this might be a good trade-off.

For the two-antenna qubit chip, several designs were proposed and evaluated. Designs

c*) and d*) look particularly promising since they both provide a large coupling, a high quality factor and by their orientation in the cavity, they offer the possibility to move the two HBAR chips further apart along the long side of the cavity. This might be important when actually building the $\hbar$BAR because the chip edges are rough after cutting and might have high dielectric losses, so they should not be too close to the Josephson Junction. Because there are spacers and glue dots at the corners of the HBAR chips, design d*) might be preferred where the antennas have a larger distance to the glue.

As mentioned already, some numbers of this thesis, especially the dielectric loss rates and relaxation times, have a high uncertainty because the loss tangents are not well known. We do not exactly know what elements the surface layers consist of and also for the bulk materials that we do know, the actual loss tangents might be different by more than an order of magnitude from the literature values assumed here for the simulations. So the findings of this thesis should be considered more in a qualitative way rather than a quantitative way. Further research should be done do determine the composition of the surface layers and to precisely quantify the loss tangents of the actual materials we use. Some designs that seem promising like transmons with a larger left pad and domes with an additional metal layer are currently fabricated and will be analyzed in more detail soon. Also a two-antenna qubit with two HBAR chips should be fabricated to compare the predicted behaviour with actual measurements.

Other aspects that could be improved in the simulation include that currently, the capacitance is calculated as $C = e^2/2E_C$ with $E_C = \hbar\alpha$ which is only an approximation in the transmon regime [15]. It would be good to include another calculation from the actual simulation to find the capacitance independent on the anharmonicity. Also, our way of calculating the dielectric surfaces losses is not the most exact. We perform surface integrals and multiply by the estimated thickness of the surface layers. But because electric charges concentrate on the edges of a conductor, the electric field strength diverges on the edges of the qubit and the simulated electric field strength might not be accurate enough at the edges due to the finite meshing size. A more sophisticated approach is presented in [23] where a coarse 3D simulation is combined with fine cross-sectional simulations of representative smaller regions.

Appendix A

Additional simulation results

Sweeping the chip spacing

In our current ħBARs, the two sapphire chips are 2.2 µm apart while the piezo has a thickness of approximately 1 µm and the part of the dome from sapphire also has a thickness of roughly 1 µm. So the distance between qubit chip and piezo dome is approximately 0.2 µm. We expect that for a larger chip spacing, there is less sapphire as a dielectric around the superconducting circuit, so its capacitance should decrease. This should increase the qubit frequency and anharmonicity and decrease the ratio E_J/E_C. This is what the simulation confirms, as shown in figure A.1. Because the chip spacing is already rather small, most data points in the simulation come from larger chip spacings. For a larger chip spacing, the piezo is farther away from the antenna, so the electric field at the piezo is smaller and therefore the participation ratio decreases. The decreased dielectric losses lead to larger T_1 times. For a very large chip spacing, this configuration corresponds to having only a qubit and no HBAR chip.

When weighing up the advantages and drawbacks for small and large chip spacings, we choose a rather small chip spacing in order to have a high coupling strength, although this causes lower T_1 times. The dispersive shift and the anharmonicity are also reduced for small chip spacings but still good for our application.

Sweeping the left pad width

As for the right pad width, also larger left pad widths increase the capacitance of the qubit. This increases the E_J/E_C ratio and decreases the qubit frequency and anharmonicity as shown in figure A.2. But in contrast, now the electric field strength increases at the antenna and at the piezo with larger left pad widths. This leads to an increase in the coupling strength. The loss rate at the piezo also increases but the loss rate of the left pad decreases by comparable amounts so that the limit on the T_1 time from dielectric losses does not change much. For small left pad widths, the dispersive shift is strongly increasing. This is because it depends on Δ and α as described in equation (2.13) and Δ decreases due to the increased qubit frequency and α increases for smaller left pad widths.

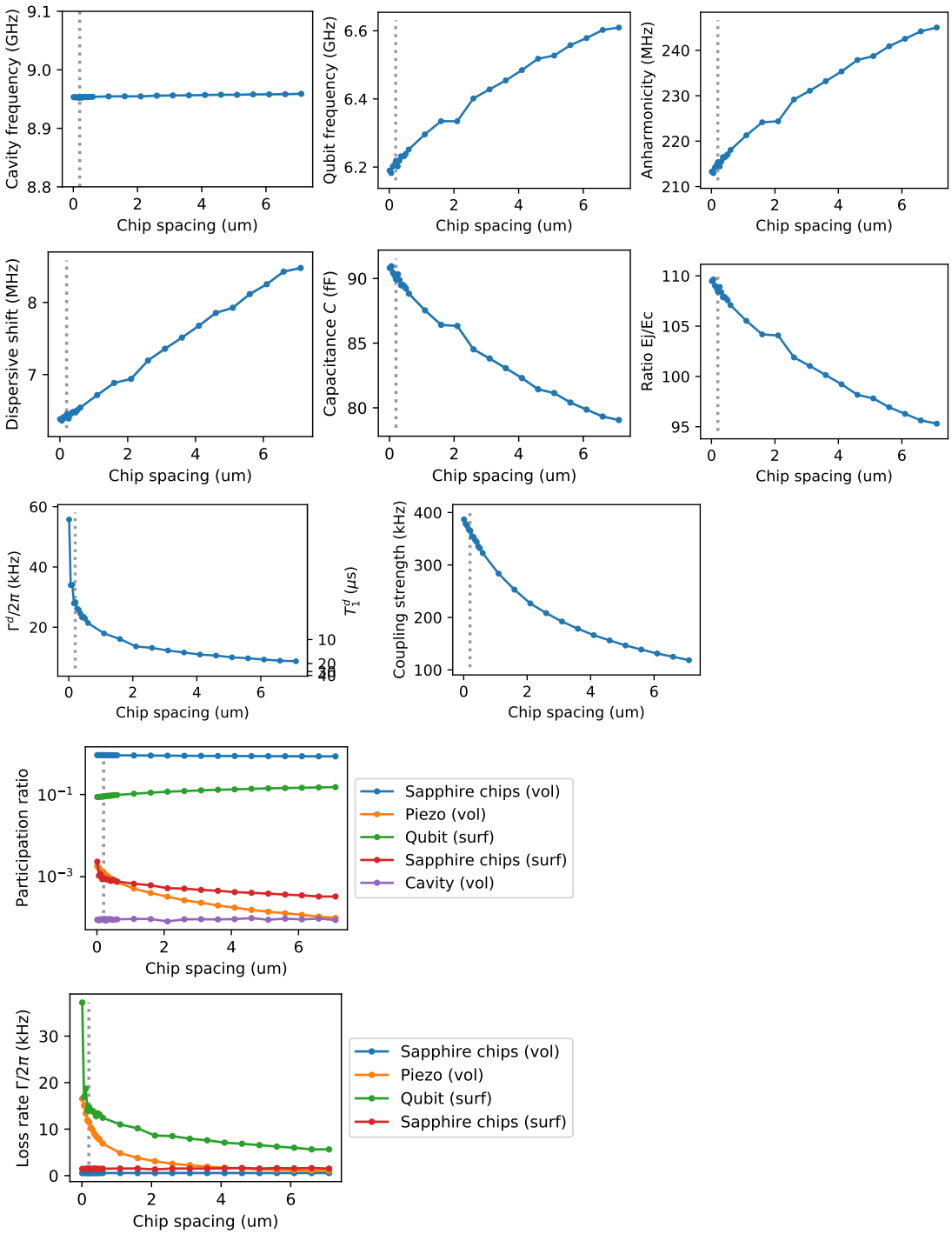

Figure A.1: Qubit parameters for the sweep of the chip spacing. Since the qubit chip and the piezo dome are currently only 0.2 µm apart, their spacing cannot be reduced much further, so most data points show larger chip spacings. A larger spacing causes less dielectric to be around which reduces the capacitance. Farther separating antenna and piezo reduces the coupling.

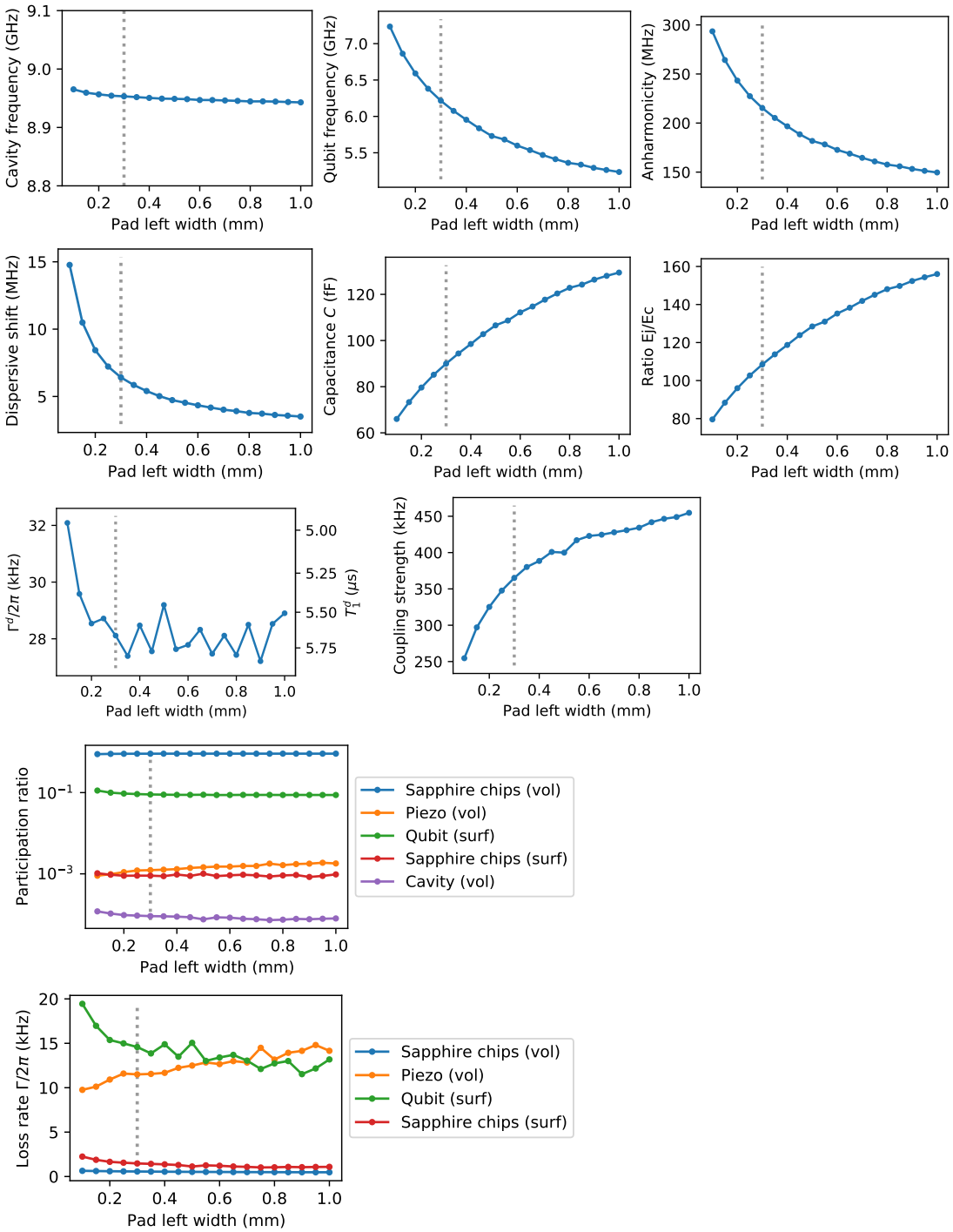

Figure A.2: Qubit parameters for the left pad width sweep.

Sweeping the antenna radius

Varying the antenna radius has no large influence on most parameters as seen in figure A.3. Only the dispersive shift and the coupling rate increase significantly with larger antenna radii. For the coupling strength calculation, it is important to change the *phonon radius* as well. We want to couple to the $(0, 0)$ Hermite-Gaussian mode which has an amplitude that follows a Gaussian distribution in the plane of the qubit. By *phonon radius* we mean the standard deviation of this Gaussian distribution. If one only changes the antenna radius without changing the phonon radius in the simulation, it is obvious that the largest coupling strength is achieved when the two radii are the same. As default values for all other sweeps, we use an antenna radius of 25 µm and a phonon radius of 25.8 µm. In this sweep of the antenna radius, we change the phonon radius in the same relative amount so that it is always 3.2 % larger than the antenna radius. Physically, this means that for a different antenna radius, one also has to change the radius of curvature of the HBAR dome which defines the phonon radius.

While not plotted here, it is clear that the energy participation ratio of the antenna increases if it increases in size compared to the rest of the circuit. The piezo dome is much larger than the antenna and the two chips are close to each other. So most of the energy from the antenna is transferred to the HBAR, independent on the antenna radius as long as it is significantly smaller than the piezo radius. Therefore, with increasing radius and energy participation ratio, also the coupling strength to the phonon mode increases. Since there are more charges located on the antenna for larger radii, the dipole moment and therefore the dispersive shift increase with increasing antenna radius.

Sweeping the antenna length

One expects that for larger antenna lengths, the dipole moment and therefore the dispersive shift increase. This is confirmed by the simulations, as seen in figure A.4. The simulations show that the capacitance is increased, so the qubit frequency and the anharmonicity decrease and the ratio of Josephson energy and capacitive energy increases. The cavity frequency does not change much as in all sweeps here.

For increased antenna lengths, we expect that the electric field at the antenna is weaker and therefore the participation ratios of antenna and piezo dome become smaller. This is indeed true after a peak of the participation ratio at 0.4 mm. For small antenna lengths below this threshold, the participation ratio of the antenna and the piezo dome increase with increasing antenna length. Probably this is due to more complex interactions between the right transmon pad and the antenna which decrease the electric field strength at the antenna or change its direction to be less perpendicular to the piezo surface. The loss rate of the piezo is proportional to its EPR and therefore has the same peak. Correspondingly, the qubit relaxation time has a minimum at 0.4 mm. The coupling strength depends on the strength of the electric field at the antenna and its direction and therefore also has a maximum at roughly 0.4 mm.

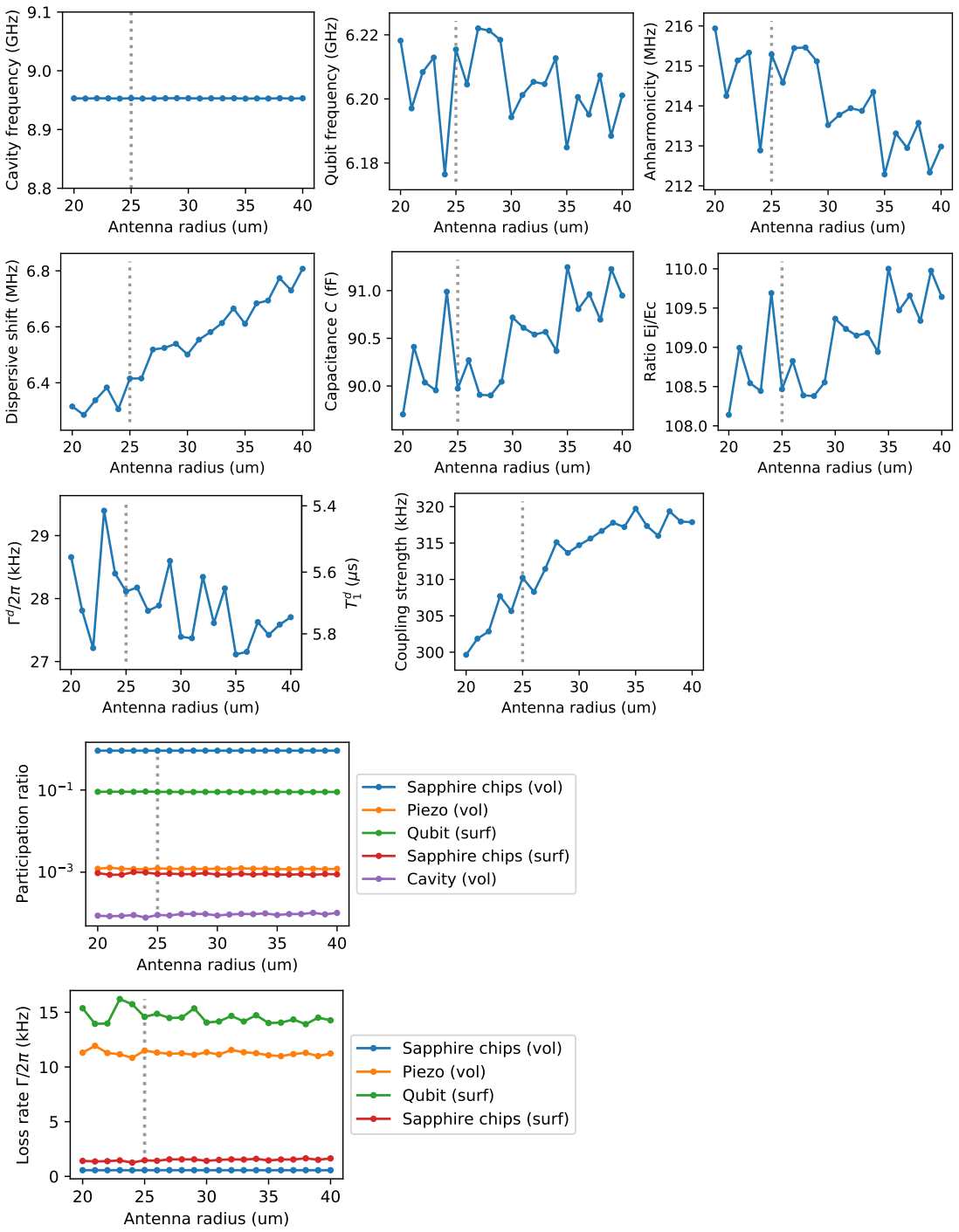

Figure A.3: Qubit parameters for the antenna radius sweep. Note the scale of the plots: Only the coupling strength changes largely with the antenna radius. All other parameters change only very little. For the coupling strength calculation, the phonon radius is set to 1.032 times the antenna radius for all simulation data points.

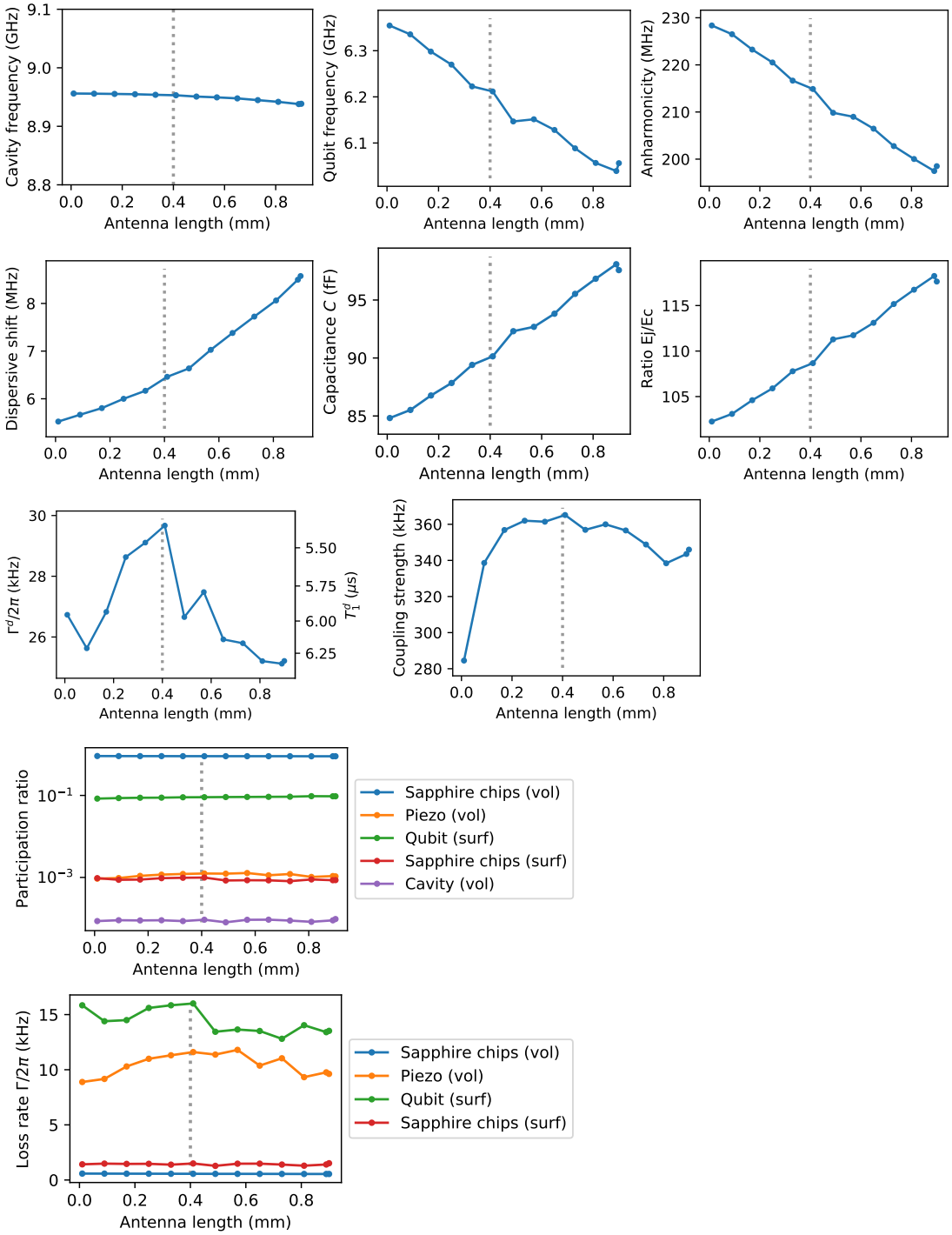

Figure A.4: Qubit parameters for the antenna length sweep.

Sweeping the antenna line width

The antenna line width has no significant effect on most parameters of the qubit. The only effect is a reduction in the coupling strength for larger widths because the electric field gets stronger at the antenna line and weaker at the actual antenna. This can again be seen in more detail when looking at an animation of the electric field when changing the antenna width in time. Therefore it is beneficial to choose the antenna line width as small as possible.

Sweeping the piezo radius

Changing the piezo radius does not influence any of the qubit parameters significantly as shown in figure A.6. The electric field strength falls off fast when moving away from the circular antenna but there is still some non-negligible electric field around the antenna. Therefore, for larger piezo radii, also the energy stored in the piezo volume increases and with that the dielectric loss rate increases and the limit on the T_1 time by dielectric losses decreases. So, decreasing the piezo radius is beneficial for the qubit decoherence time. But with a beam propagation simulation, one needs to check how this influences the phonon decoherence time since reducing the piezo radius corresponds to cutting of the tails of the Gaussian beam.

Sweeping the piezo thickness

Varying the thickness of the piezo between 0.5 µm and 1.5 µm does not change most of the qubit parameters as seen in figure A.7. However, the EPR and the loss rate are increasing as expected with larger thickness and therefore the T_1 time is decreasing. The most important effect is that the coupling strength varies greatly. It is maximal when the thickness is half the wavelength $\lambda/2 = c_s/f_q \approx 0.9\,\mu\text{m}$ where we assume a speed of sound in sapphire of $c_s = 1.1157 \cdot 10^4\,\text{m}\,\text{s}^{-1}$ and a qubit frequency of $f_q = 6.2\,\text{GHz}$. At this thickness, the boundary conditions are optimal for a standing wave with two nodes at both ends and one antinode in the middle which leads to the highest coupling strength. When further increasing the thickness, standing waves are also created for thicknesses of $\lambda, \frac{3}{2}\lambda, 2\lambda$, etc. But for integer multiples of λ, the modes have an even number of antinodes so the integral of stress times strain is an integral of a sine over one or several complete periods which is just zero. Only for half-integer multiples of λ, the number of antinodes is uneven and the integral is maximal.

Sweeping the pad distance

Increasing the pad distance d leads to a higher dipole moment and therefore to a higher dispersive shift.

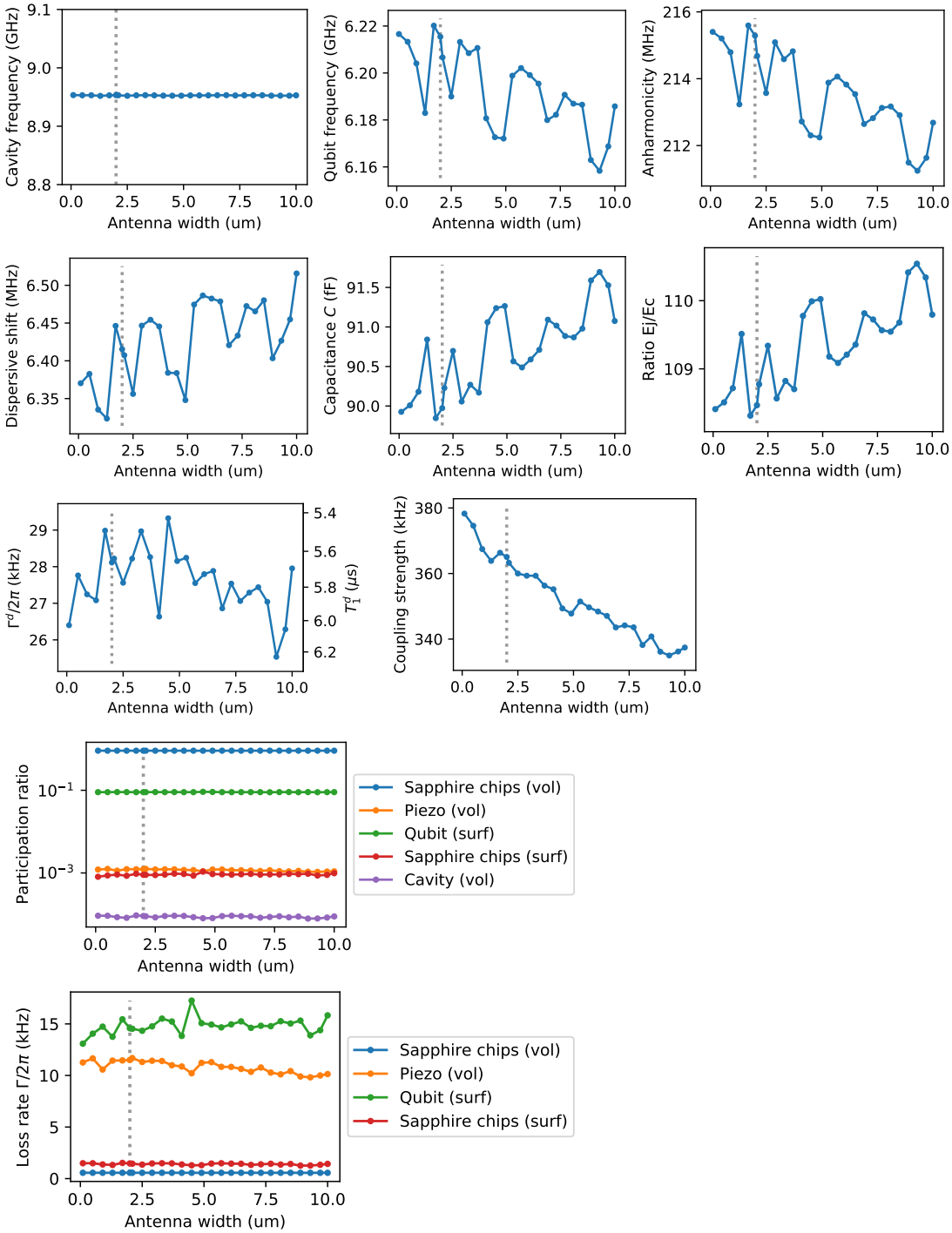

Figure A.5: Qubit parameters for the antenna line width sweep.

Sweeping the JJ inductance

Above in section 3.2 we showed that we can easily change the qubit frequency to a value we want by changing the inductance of the Josephson Junction. This is plotted here in more detail by sweeping the inductance from 2 nH to 10 nH.

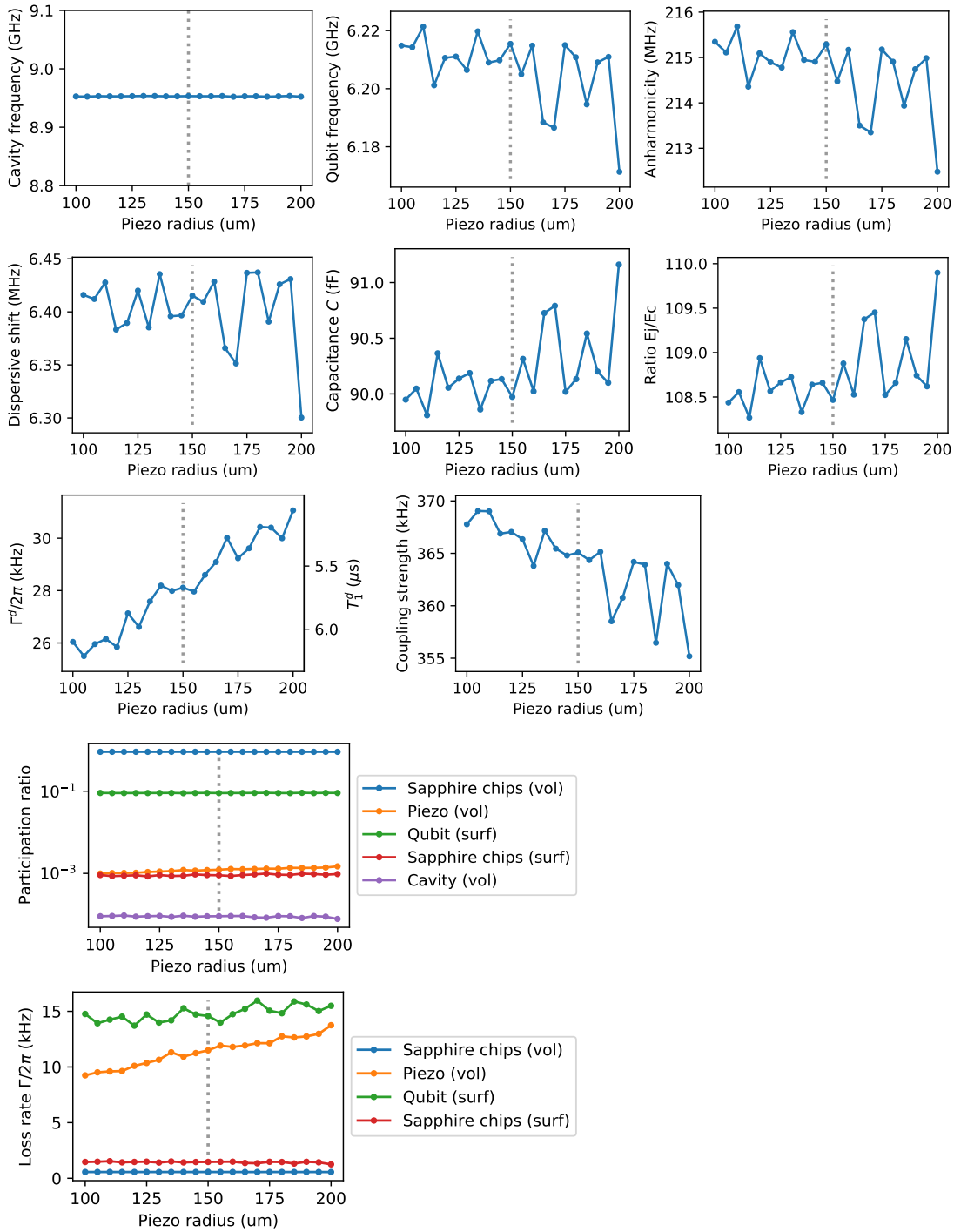

Figure A.6: Qubit parameters for the piezo radius sweep.

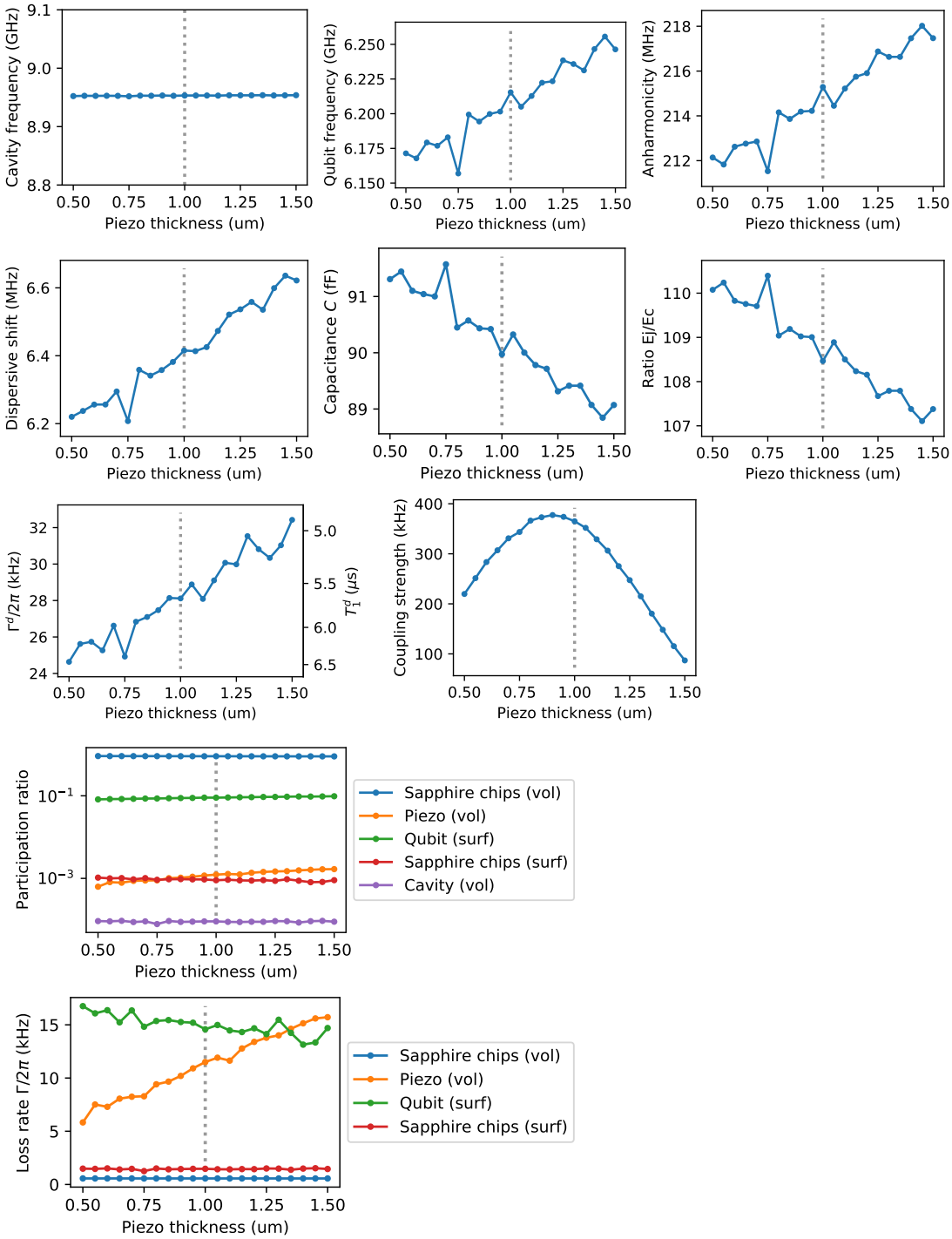

Figure A.7: Qubit parameters for the piezo thickness sweep.

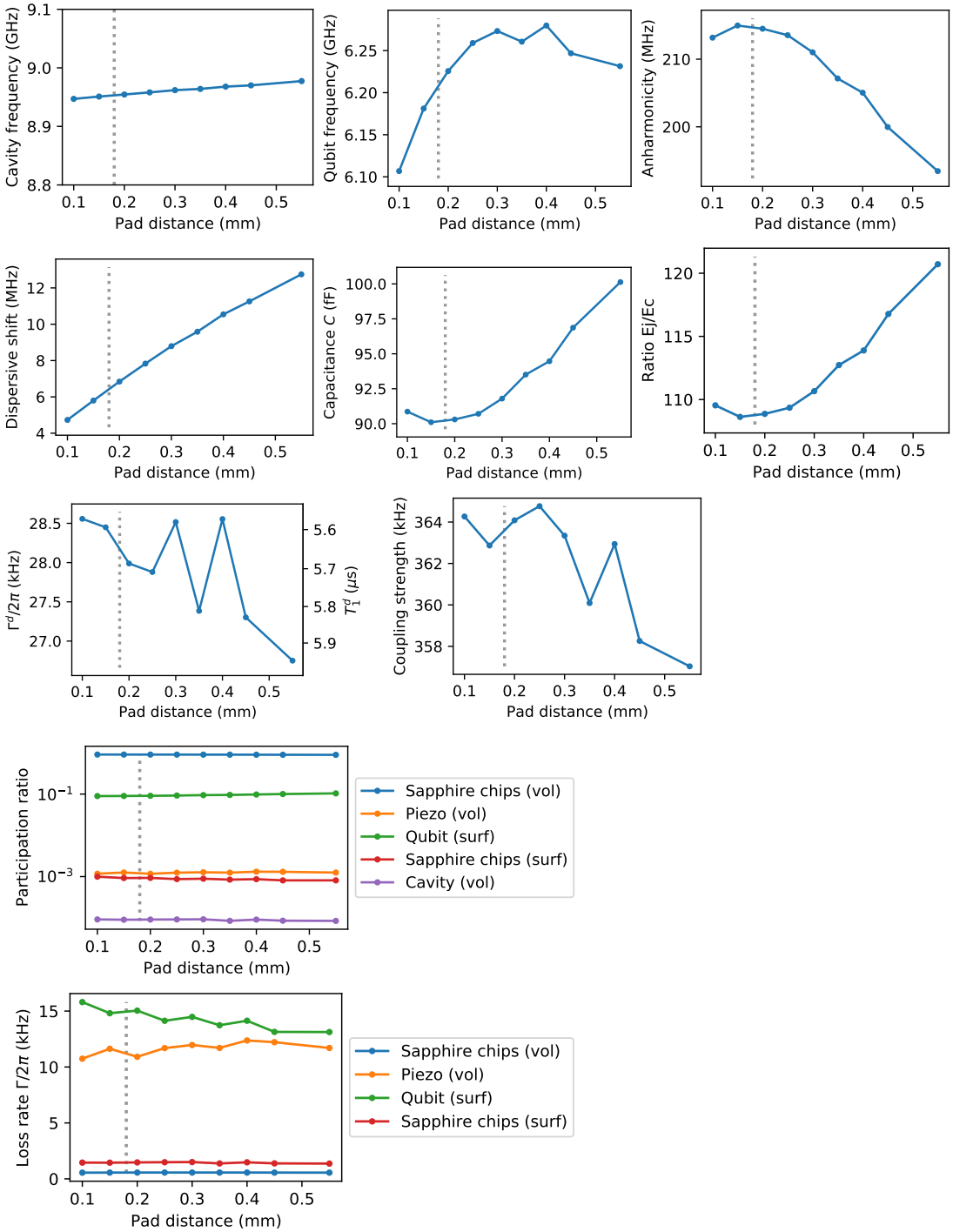

Figure A.8: Qubit parameters for the pad distance sweep.

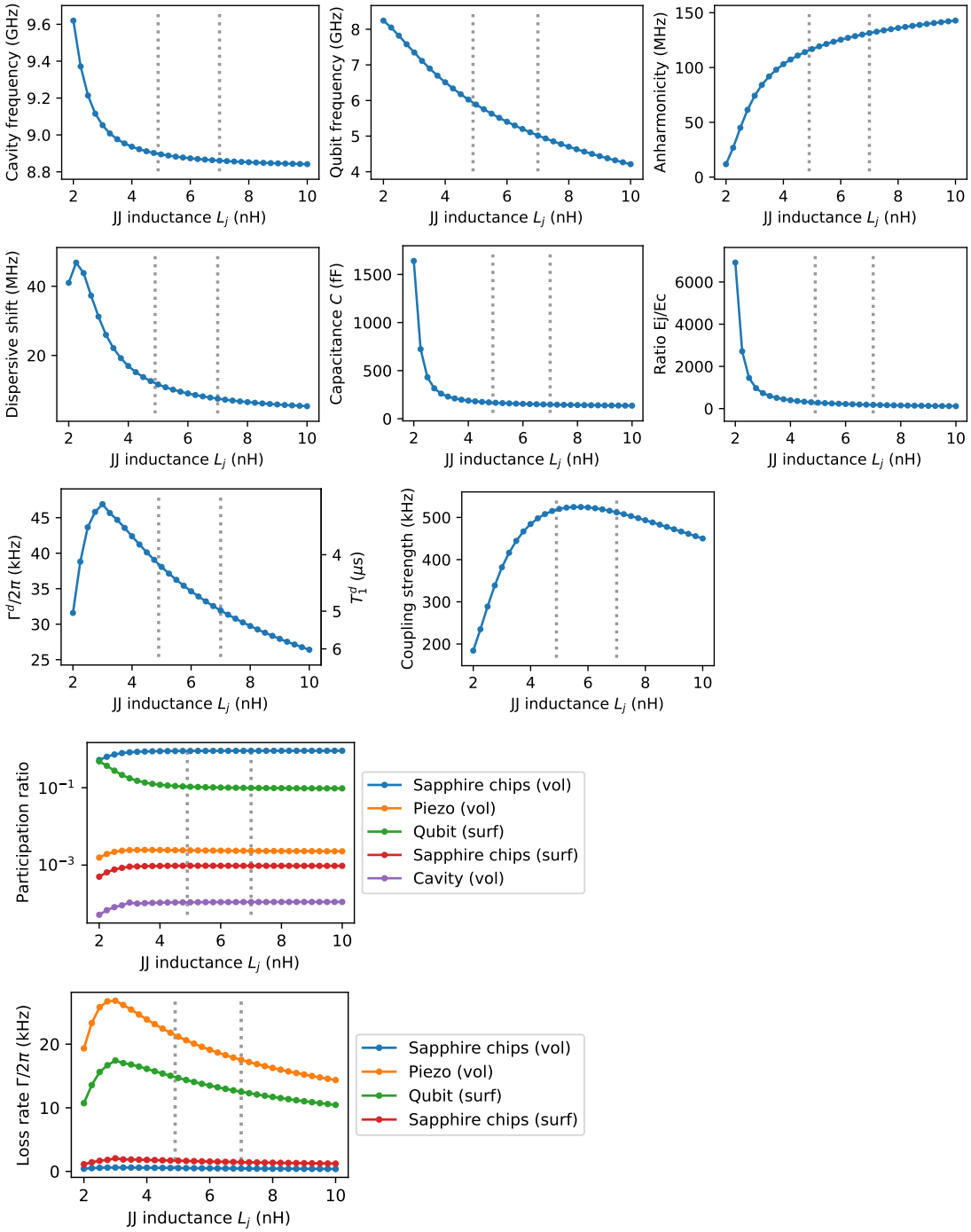

Figure A.9: Qubit parameters for the JJ inductance sweep. By changing the inductance, we can tune the qubit frequency to a desired value.

Appendix B

Defining parametric surfaces in Ansys

Simple geometric surfaces like rectangles and ellipses can easily be drawn in Ansys. More complex surfaces can be modelled with the parametric surface feature in Ansys. During this project, this was used for modelling the funnels and the curved antennas in the 2-HBAR design. For reproducing the model or applying the same technique to other surfaces, the formulas are explained here.

Bézier curves

The funnels in our qubit design can be modelled with the help of Bézier curves. The points of a Bézier curve in two dimensions are given in vector notation by

$$\mathbf{B}(u) = (1-u)^3\mathbf{P}_0 + 3(1-u)^2u\mathbf{P}_1 + 3(1-u)u^2\mathbf{P}_2 + u^3\mathbf{P}_3, \quad 0 \leq u \leq 1. \tag{B.1}$$

This can be written as two equations for the x and y component:

$$x(u) = (1-u)^3x_0 + 3u(1-u)^2x_1 + 3u^2(1-u)x_2 + u^3x_3 \tag{B.2}$$

$$y(u) = (1-u)^3y_0 + 3u(1-u)^2y_1 + 3u^2(1-u)y_2 + u^3y_3 \tag{B.3}$$

with 8 parameters $x_{0,1,2,3}$ and $y_{0,1,2,3}$, specifying the position and shape of the Bézier curve. In our case, we want the curve to go from $P_0 = (0, y_0)$ to $P_3 = (1, 1)$ and we use the parameter s as kind of the "curvature" of the curve, i.e. we want $P_1 = (s, y_0)$ and $P_2 = (1-s, 1)$. Then

$$x(u) = 3u(1-u)^2s + 3u^2(1-u)(1-s) + u^3 \tag{B.4}$$

$$y(u) = 3u(1-u)^2y_0 + 3u^2(1-u) + u^3. \tag{B.5}$$

In our qubit design, the funnels are each enclosed by two Bézier curves mirrored at the x axis, so in Ansys we let the second parameter v go from -1 to $+1$ and multiply y by v. By that we get the complete surface between the two mirrored Bézier curves.

Annulus

For the curved part of the antenna in the 2-HBAR design, we want to draw a quarter of an annulus with thickness (in radial direction) of d and mean radius r. So the radius of the inner circle of the annulus should be $r - d/2$ and the radius of the outer circle $r + d/2$. We use the variable $u \in [-1, 1]$ for describing the current thickness of the annulus, so with $r + d \cdot u/2$ this variable u is mapped to the interval $[r - d/2, r + d/2]$. The variable $v \in [0, 1]$ is mapped to the angle $\varphi \in [0, \pi/2]$ as $\varphi = \pi/2 \cdot v$. The x and y component of every point of the annulus can just be taken as $x = (r + d \cdot u/2) \cdot \cos(\pi/2 \cdot v)$ and $y = (r + d \cdot u/2) \cdot \sin(\pi/2 \cdot v)$.

Bibliography

1. Nielsen, M. A. & Chuang, I. L. *Quantum Computation and Quantum Information: 10th Anniversary Edition* 10th. ISBN: 1107002176 (Cambridge University Press, USA, 2011).
2. Chu, Y. *et al.* Quantum acoustics with superconducting qubits. *Science* **358,** 199–202. eprint: https://www.science.org/doi/pdf/10.1126/science.aao1511. https://www.science.org/doi/abs/10.1126/science.aao1511 (2017).
3. Chu, Y. *et al.* Creation and control of multi-phonon Fock states in a bulk acoustic-wave resonator. *Nature* **563,** 666–670. ISSN: 1476-4687. http://dx.doi.org/10.1038/s41586-018-0717-7 (Nov. 2018).
4. Kharel, P. *et al.* Ultra-high-Q phononic resonators on-chip at cryogenic temperatures. arXiv: 1803.10077 [physics.optics] (2018).
5. Von Lüpke, U. *et al.* Parity measurement in the strong dispersive regime of Circuit Quantum acoustodynamics. *Nature Physics.* https://www.nature.com/articles/s41567-022-01591-2 (May 2022).
6. Minev, Z. K. *et al. pyEPR: The energy-participation-ratio (EPR) open- source framework for quantum device design* May 2021. https://doi.org/10.5281/zenodo.4744447.
7. Seis, Y. *et al.* Ground state cooling of an ultracoherent electromechanical system. en. *Nature Communications* **13,** 1507. ISSN: 2041-1723. https://www.nature.com/articles/s41467-022-29115-9 (2022) (Dec. 2022).
8. Hann, C. T. *et al.* Hardware-Efficient Quantum Random Access Memory with Hybrid Quantum Acoustic Systems. *Physical Review Letters* **123.** https://doi.org/10.1103%2Fphysrevlett.123.250501 (Dec. 2019).
9. Cochrane, P. T., Milburn, G. J. & Munro, W. J. Macroscopically distinct quantum-superposition states as a bosonic code for amplitude damping. *Physical Review A* **59,** 2631–2634. https://doi.org/10.1103%2Fphysreva.59.2631 (Apr. 1999).
10. Leghtas, Z. *et al.* Hardware-Efficient Autonomous Quantum Memory Protection. *Physical Review Letters* **111.** https://doi.org/10.1103%2Fphysrevlett.111.120501 (Sept. 2013).
11. Mirrahimi, M. *et al.* Dynamically protected cat-qubits: a new paradigm for universal quantum computation. *New Journal of Physics* **16,** 045014. https://doi.org/10.1088%2F1367-2630%2F16%2F4%2F045014 (Apr. 2014).
12. Gottesman, D., Kitaev, A. & Preskill, J. Encoding a qubit in an oscillator. *Physical Review A* **64.** https://doi.org/10.1103%2Fphysreva.64.012310 (June 2001).

13. Albert, V. V. *et al.* Performance and structure of single-mode bosonic codes. *Physical Review A* **97.** https://doi.org/10.1103%2Fphysreva.97.032346 (Mar. 2018).

14. Knoll, J. Automated transmon characterization with pyEPR. https://github.com/JONA-X/hyqu-qubit-simulation (Apr. 2022).

15. Koch, J. *et al.* Charge-insensitive qubit design derived from the Cooper pair box. *Physical Review A* **76.** ISSN: 1094-1622. http://dx.doi.org/10.1103/PhysRevA.76.042319 (Oct. 2007).

16. Krantz, P. *et al.* A quantum engineer's guide to superconducting qubits. *Applied Physics Reviews* **6,** 021318. eprint: https://doi.org/10.1063/1.5089550. https://doi.org/10.1063/1.5089550 (2019).

17. Kittel, C. *Introduction to Solid State Physics* ISBN: 9780471415268 (Wiley, 2004).

18. Tinkham, M. *Introduction to Superconductivity* 2nd ed. ISBN: 0486435032. http://www.worldcat.org/isbn/0486435032 (Dover Publications, June 2004).

19. Ambegaokar, V. & Baratoff, A. Tunneling Between Superconductors. *Phys. Rev. Lett.* **10,** 486–489. https://link.aps.org/doi/10.1103/PhysRevLett.10.486 (11 June 1963).

20. Park, G. *et al.* Observation of a Strongly Enhanced Relaxation Time of an In-situ Tunable Transmon on a Silicon Substrate up to the Purcell Limit Approaching 100 μs. *Journal of Korean Physical Society* **76,** 1029–1034 (June 2020).

21. Blais, A., Grimsmo, A. L., Girvin, S. & Wallraff, A. Circuit quantum electrodynamics. *Reviews of Modern Physics* **93.** https://doi.org/10.1103%2Frevmodphys.93.025005 (May 2021).

22. Blais, A., Huang, R.-S., Wallraff, A., Girvin, S. M. & Schoelkopf, R. J. Cavity quantum electrodynamics for superconducting electrical circuits: An architecture for quantum computation. *Phys. Rev. A* **69,** 062320. https://link.aps.org/doi/10.1103/PhysRevA.69.062320 (6 June 2004).

23. Wang, C. *et al.* Surface participation and dielectric loss in superconducting qubits. arXiv: 1509.01854v2 (2015).

24. Creedon, D. L. *et al.* High Q-factor sapphire whispering gallery mode microwave resonator at single photon energies and millikelvin temperatures. *Applied Physics Letters* **98,** 222903. eprint: https://doi.org/10.1063/1.3595942. https://doi.org/10.1063/1.3595942 (2011).

25. O'Connell, A. D. *et al.* Microwave dielectric loss at single photon energies and millikelvin temperatures. *Applied Physics Letters* **92,** 112903. eprint: https://doi.org/10.1063/1.2898887. https://doi.org/10.1063/1.2898887 (2008).